J. Fluid Mech. (1991), *vol.* 228, *pp.* 111–148
Printed in Great Britain

Three-dimensional wavelike equilibrium states in plane Poiseuille flow

By U. EHRENSTEIN† AND W. KOCH
DLR Institute for Theoretical Fluid Mechanics, D-3400 Göttingen, Germany

(Received 9 April 1990)

In the quest for a physically more realistic transition criterion, the prechaotic bifurcation behaviour of plane Poiseuille flow is studied. Various classes of nonlinear time-periodic equilibrium solutions are computed via Keller's pseudo-arclength continuation method. In particular, attention is focused on three-dimensional nonlinear travelling-wave type secondary bifurcation branches. These saturated equilibrium states originate on the nonlinear primary bifurcation surface from neutral, phase-locked secondary instability modes. Taking advantage of symmetries, only those nonlinear secondary branches which correspond to symmetric and antisymmetric linear secondary instability modes are investigated.

It appears that a new family of secondary bifurcation solutions which contains only even spanwise Fourier modes is particularly important. Dominated largely by the spanwise (0, 2) mode and discovered by investigating bicritical secondary bifurcations, the mean quantities of these solutions show a certain resemblance to those observed in transitional flow during the 'spike' stage. The friction factor of this new solution branch is in the experimentally observed range and the critical Reynolds number, defined with the mean flow velocity, is reduced to about 1000 in general agreement with experiments.

1. Introduction

The transition from smooth and steady laminar flow to the random and chaotic motion of turbulent flow is one of the central problems in fluid mechanics. The transition problem became of increased practical importance for the design of a laminar flow controlled (LFC), swept-wing transport aircraft. By delaying boundary-layer transition, considerable performance increases can be achieved. Prerequisite for such an advanced design is an in-depth understanding of the underlying physical process together with a reliable and accurate method for predicting laminar/turbulent transition with and without LFC. Carefully conducted experiments as well as the use of high-speed computers significantly advanced our understanding of this fascinating phenomenon as can be seen from the overviews by Tani (1969), Stuart (1971), Reshotko (1976), AGARD-CP-224 (1977), Morkovin (1988), Herbert (1988) and Reed & Saric (1989), as well as the proceedings of the IUTAM symposia on laminar–turbulent transition.

However this rather detailed understanding of the transition process has not yet been incorporated in design-type transition prediction methods. Essentially all engineering transition prediction methods presently in use are based upon linear primary instability in conjunction with a correlation of transition information

† Present address: Institut Français du Pétrole, F-92506 Rueil Malmaison Cedex, France.

obtained from experiments (so-called e^N methods, cf. Bushnell, Malik & Harvey 1989). Used with care, these semi-empirical prediction methods seemingly work quite well in many situations of engineering interest. Although transition is a nonlinear process, apparently the very rapidity of this nonlinear process allows the neglect of nonlinearity in these situations, being the reason behind the success of the e^N approach in low-disturbance environments. However, besides providing little physical insight, the failure of these semi-empirical methods in cases where the linear stage is bypassed, such as Poiseuille flow, makes their application to new design situations hazardous unless backed up by extensive experimental data. Therefore, a physically more rational transition prediction method, which includes bypass situations and does not require empirical constants, is one of the main goals of present-day transition research.

The object of this investigation is to study the prechaotic bifurcation behaviour of strongly nonlinear, wavelike (i.e. time-periodic) equilibrium solutions for the model problem of plane Poiseuille flow. In particular we hope to find some clues as to whether these solutions can be related to the advanced stages of transition and therefore could be used for transition prediction in engineering problems. At the same time our strongly nonlinear solutions elucidate the validity and interrelations between various weakly nonlinear models and offer a possible explanation for the drag reducing effect of riblets. While the ultimate goal of finding a better transition criterium is not achieved in this paper, a new class of secondary bifurcation solutions containing only even spanwise modes brings the critical Reynolds number as well as the friction factor into the experimentally observed range.

1.1. *Historical background; weakly nonlinear theories*

Osborne Reynolds attributed laminar/turbulent transition to an instability of the flow. The theoretical development of classical *linear primary stability theory*, initiated by Rayleigh, Kelvin and Helmholtz for inviscid flows and extended to viscous flows by Orr and Sommerfeld is nicely summarized in the monograph of Drazin & Reid (1981). The theoretical predictions of Tollmien (1929) and Schlichting (1933) of travelling instability waves in the Blasius boundary layer were confirmed beautifully by the landmark experiment of Schubauer & Skramstad (1947). Discrepancies between linear stability results and experimentally observed transition were attributed to nonlinear effects. Because two-dimensional Tollmien–Schlichting (TS) waves experience amplification at the lowest Reynolds number (cf. Squire 1933), historically nonlinear extensions centred on two-dimensional waves. Using an amplitude expansion technique, Stuart (1960) and Watson (1960) formally derived *Landau's equation* as the equation governing the temporal evolution of weakly nonlinear two-dimensional disturbances near the critical point (compare also Stuart's 1971 review).

A critical survey of the various weakly nonlinear two-dimensional amplitude expansion methods has been given by Herbert (1983), who also demonstrated the disappointingly limited range of validity of these amplitude expansions for the example of plane Poiseuille flow in his earlier paper (cf. Herbert 1980). Therefore, in the opinion of the present authors the main value of these weakly nonlinear theories appears to be the accurate prediction of the local bifurcation behaviour, in particular whether the bifurcation is supercritical or subcritical.

On the other hand, experimental investigations of Klebanoff, Tidstrom & Sargent (1962) clearly demonstrated that the linearly most amplified two-dimensional TS waves quickly became three-dimensional, forming aligned Λ-shaped vortical patterns before the fully turbulent stage was reached. To explain this observed peak–valley splitting of what is now known as *harmonic* or *K-type transition*, Benney & Lin (1960) and later Benney (1964) proposed weakly nonlinear interactions between a two-dimensional TS wave $(\alpha, 0)$ and two non-resonant oblique waves $(\alpha, \pm\beta)$. Here α and β denote the streamwise and spanwise wavenumbers. Aside from some debatable assumptions regarding the phase, this model provided no selection mechanism for the preferred spanwise periodicity of the streamwise vortices. To remedy this, Craik (1971) introduced his *resonant triad* model which exploits the resonance between a two-dimensional TS wave $(\alpha, 0)$ and two subharmonic oblique waves $(\frac{1}{2}\alpha, \pm\beta)$ (see also Craik's 1985 monograph). This resonance model did not apply to the experimental situation of Klebanoff *et al.* (1962) but found revived interest with the experimental verification of the subharmonic route to transition in boundary layers by Kachanov & Levchenko (1984) or Saric & Thomas (1984).

In contrast to the above-cited weakly nonlinear three-dimensional models, Dhanak (1983) studied finite-amplitude disturbances in the form of standing waves in a spanwise direction. These are expansions about the linear three-dimensional neutral surface and can be linked to the superharmonic resonance between a two-dimensional wave $(2\alpha, 0)$ and two oblique waves $(\alpha, \pm\beta)$ on the neutral surface. We shall use Dhanak's (1983) results for comparison with our strongly nonlinear three-dimensional solution of §3.3.

Undoubtedly one of the great achievements of theoretical transition research during the past decade has been to recognize that the rapid growth of the three-dimensional waves is due to a *linear secondary instability* of the two-dimensional primary waves after having reached a certain threshold amplitude (cf. Orszag & Patera 1980, 1983; Herbert 1981, 1988). Originating from *parametric resonance* of a periodic flow, secondary instability appears to be a generic mechanism in shear flows and the different types of parametric resonance can explain the different routes to transition (see Bayly, Orszag & Herbert 1988 or Herbert 1988). However, it should be emphasized that, although linear secondary stability theory correctly describes the onset of transition, it fails to provide a transition criterion unless experimental information is added or nonlinear effects are included. Such a weakly nonlinear secondary instability model has been proposed by Crouch & Herbert (1986) and according to the authors it describes the evolution of disturbances up to the single-spike stage showing some potential for a rational transition prediction. Our main results of §4 are also concerned with such secondary bifurcation branches and we shall see that some lead to a considerable reduction of the critical Reynolds number in agreement with experimental observations.

1.2. *Strongly nonlinear computations*

The development of new computational methods, in particular spectral methods (see Canuto *et al.* 1988), as well as advances in high-speed computers, made it possible to perform accurate, time-dependent numerical simulations of the transition process for simple model problems. The high-resolution simulations of Kim, Moin & Moser (1987) or Gilbert (1988) for plane Poiseuille flow are impressive examples of the wealth of information that can be obtained in this way (see also the review by Kleiser & Zang 1991). Even more astonishing are Rozhdestvensky & Simakin's (1984) findings, extending earlier simulation results of Orszag & Patera (1980, 1983), that a low-resolution simulation already closely approximates several overall quantities of engineering interest, such as the friction factor or the mean velocity profile. It appears that in flows which are dominated by large-scale coherent structures, the latter are adequately taken into account by such low-resolution models. This would also explain the success of Liu's (1989) highly truncated nonlinear wave-envelope method, which can be regarded as a large-amplitude extension of several weakly nonlinear models. Apparently these solutions, obtained by Fourier truncation, have a much larger region of convergence than those based upon amplitude expansions (compare for example Herbert 1980 or Sen & Venkateswarlu 1983).

The strictly parallel basic state of plane Poiseuille flow, which according to linear theory is convectively unstable (cf. Deissler 1987), admits solutions which are periodic in the streamwise and spanwise directions and much theoretical work has been expended on studying the stability of this simple flow. Therefore it constituted a milestone in transition research when, analogous to Schubauer & Skramstad's (1947) boundary-layer experiment, Nishioka, Iida & Ichikawa (1975) confirmed experimentally the results of linear and weakly nonlinear stability theory for this highly subcritical flow. Their investigation showed a close similarity between ribbon-induced transition in plane Poiseuille and boundary-layer flow, hereby firmly establishing plane Poiseuille flow as an important model problem for the study of wall-bounded shear flows.

An alternative to the evolutionary initial-value approach is a *global numerical bifurcation analysis* in the parameter space which will be employed in the present investigation. Such an approach has been applied frequently to closed flow systems such as Taylor–Couette or Rayleigh–Bénard flow (cf. for example Meyer-Spasche & Keller 1980 or Schrauf 1986). Starting with a known solution and using continuation methods (cf. Keller 1977; Doedel 1981; Kubiček & Marek 1983 or Jepson & Keller 1984), one computes the bifurcating branches of a certain solution class (usually steady or time periodic solutions). Naturally, these solutions fall short of reaching the chaotic end states obtainable by evolutionary numerical simulation. However, for closed flow systems, several of these intermediate equilibrium states are stable and can be observed experimentally. Contrary to this, most of the intermediate states of open flow systems seem to be unstable and therefore are not observed in experiments or cannot be computed easily by time-dependent numerical simulation. Nevertheless, these unstable intermediate solutions provide a highly useful insight into the transition process, as exemplified by secondary bifurcations in shear flows (cf. Herbert 1991). Furthermore, there is increasing evidence that these intermediate states might be related to the coherent structures observed in transitional and turbulent flows (cf. Saffmann 1983, who termed these intermediate solutions 'vortical states', or Liu 1989). Speaking in terms of dynamical systems theory, these coherent structures can be thought of as being lower-dimensional manifolds in whose neighbourhood the dynamical system spends a substantial fraction of time (Jiménez 1987*a*). If the flow is controlled by large-scale structures it is only natural to hypothesize (cf. Koch 1988) that mean quantities of engineering interest might be determined accurately enough by these intermediate solutions to allow a physically more rational prediction of transition.

Similar to the time-dependent simulations, progress in numerical bifurcation theory mirrors the advances in numerical methods as well as computer technology. This is particularly evident from the few results for plane Poiseuille flow, our open flow system model. Based upon the asymptotic approach of Meksyn & Stuart (1951) and Meksyn (1964), Grohne (1969) and Zahn *et al.* (1974) seem to have been the first to tackle this problem numerically. They used finite-difference methods just as Milinazzo & Saffman (1985) did later on. Using spectral methods, Herbert (1977) as well as Orszag & Kells (1980), Orszag & Patera (1983) and Pugh (1987), achieved high

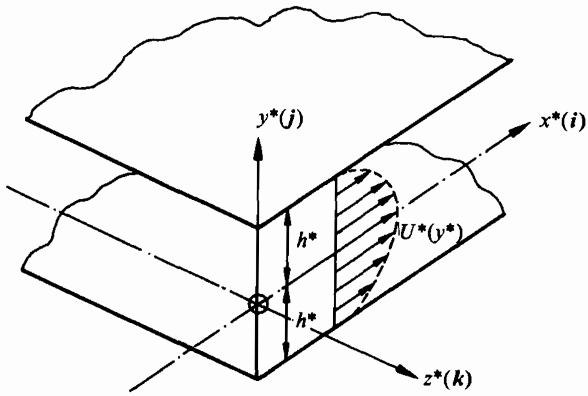

FIGURE 1. Plane Poiseuille flow geometry.

accuracy by keeping several streamwise harmonics. Most of these computations were for two-dimensional disturbances. Employing the mean-field approximation Grohne (1969) and Zahn *et al.* (1974) also reported limited results for three-dimensional disturbances. These three-dimensional calculations were continued by Pugh (1987), Koch (1988) and Ehrenstein & Koch (1989) with the particular goal of computing secondary bifurcation equilibria.

The present paper summarizes and extends the results reported in Ehrenstein & Koch (1989) and is organized as follows. Section 2 contains the governing equations and an outline of the numerical method of solution. After a brief review of three-dimensional linear and two-dimensional nonlinear primary instability, new nonlinear three-dimensional primary bifurcation results are compared with weakly nonlinear computations in §3. Section 4 contains a selected overview of linear secondary instability results and then focuses on two families of nonlinear wavelike secondary bifurcation solutions. Finally, some conclusions are drawn in §5 with a speculative comment about a possible connection between the discussed secondary bifurcation solutions and drag reducing riblets.

2. Governing equations and method of solution

2.1. *Governing equations*

The flow of an incompressible viscous fluid of constant density ρ^* between two parallel plates and driven by a pressure gradient is governed by the Navier–Stokes equations. By convention all quantities are non-dimensionalized with the maximum laminar velocity U^*_{max} at midchannel (see figure 1), the channel half width h^* and the (constant) kinematic viscosity ν^*. Then $\boldsymbol{v} \equiv (u, v, w) = \boldsymbol{v}^*/U^*_{max}$ and $p = p^*/(\rho^* U^{*2}_{max})$ are the dimensionless velocity and pressure respectively, $\boldsymbol{x} \equiv (x, y, z) = \boldsymbol{x}^*/h^*$ denotes the Cartesian coordinates in the streamwise, normal and spanwise direction, with the corresponding unit vectors $(\boldsymbol{i}, \boldsymbol{j}, \boldsymbol{k})$ and $Re = U^*_{max} h^*/\nu^*$ is the Reynolds number. Furthermore $\boldsymbol{\omega} \equiv (\xi, \eta, \zeta) = \boldsymbol{\nabla} \times \boldsymbol{v}$ denotes the vorticity vector and a streamfunction vector $\boldsymbol{\psi}$ can be introduced by $\boldsymbol{v} = \boldsymbol{\nabla} \times \boldsymbol{\psi}$.

To allow a better comparison with weakly nonlinear theories it is customary to write

$$\boldsymbol{v}(x, y, z, t) = U(y)\, \boldsymbol{i} + \epsilon \tilde{\boldsymbol{v}}(x, y, z, t),$$

$$p(x, y, z, t) = P(x) + \epsilon \tilde{p}(x, y, z, t),$$

$$\boldsymbol{\omega}(x, y, z, t) = \boldsymbol{\Omega}(y)\, \boldsymbol{k} + \epsilon \tilde{\boldsymbol{\omega}}(x, y, z, t).$$

Here $U(y) = 1-y^2$, $P(x) = -2x/Re$ and $\Omega(y) = 2y$ describe the steady laminar flow and all disturbance quantities are marked by a tilde. ϵ is an amplitude which can be large and will be specified later by a normalization condition. Since we are interested in travelling-wave type solutions it is advantageous to transform the equations of motion into a frame of reference moving with the (unknown) wave speed C in the x-direction, i.e. $x' = x-Ct$, $y' = y$, $z' = z$, $t' = t$ and dropping the prime from now on. In our treatment we chose the normal velocity $\tilde{v}$ and the normal vorticity $\tilde{\eta}$ as independent variables such that the governing equations can be written in the form

$$\left\{\frac{\partial}{\partial t}+(U-C)\frac{\partial}{\partial x}-\frac{1}{Re}\nabla^2\right\}\nabla^2\tilde{v}+\frac{\mathrm{d}\Omega}{\mathrm{d}y}\frac{\partial\tilde{v}}{\partial x}$$
$$+\epsilon\left\{\frac{\partial}{\partial x}[(\tilde{v}\cdot\nabla)\tilde{\zeta}-(\tilde{\omega}\cdot\nabla)\tilde{w}]-\frac{\partial}{\partial z}[(\tilde{v}\cdot\nabla)\tilde{\xi}-(\tilde{\omega}\cdot\nabla)\tilde{u}]\right\}=0, \quad (1)$$

$$\left\{\frac{\partial}{\partial t}+(U-C)\frac{\partial}{\partial x}-\frac{1}{Re}\nabla^2\right\}\tilde{\eta}-\Omega\frac{\partial\tilde{v}}{\partial z}+\epsilon[(\tilde{v}\cdot\nabla)\tilde{\eta}-(\tilde{\omega}\cdot\nabla)\tilde{v}]=0. \quad (2)$$

To specify the solution uniquely, usually the pressure gradient (or equivalently the wall shear stress) or the mass flux is held constant (cf. Saffmann 1983 or Rozhdestvensky & Simakin 1984). For laminar flow both formulations are identical, but different results are obtained in transitional or turbulent flow. In our work we have chosen the constant pressure gradient formulation, i.e. $Re \equiv Re_p = U^*_{\max_p} h^*/\nu^*$, in order to allow a better comparison with most previous publications even though in experiments in general the constant flux formulation $Re \equiv Re_Q = U^*_{\max_Q} h^*/\nu^*$ is realized. To complete the formulation of our model problem we impose the no-slip boundary condition

$$\tilde{v}(x, y=\pm 1, z, t) = 0,$$

on the bounding sidewalls.

2.2. *Modal expansions and symmetries*

As mentioned before we are interested in travelling-wave type equilibrium solutions. In the frame of reference moving with the wave these solutions are stationary, i.e. $\partial/\partial t \equiv 0$. Furthermore, plane Poiseuille flows allows solutions which are periodic in the streamwise and spanwise directions and therefore can be expressed in terms of the *modal expansion*

$$\begin{Bmatrix}\tilde{v}(x,y,z)\\ \tilde{\omega}(x,y,z)\end{Bmatrix}=\sum_{n=-\infty}^{\infty}\sum_{m=-\infty}^{\infty}\begin{Bmatrix}\hat{v}_{nm}(y)\\ \hat{\omega}_{nm}(y)\end{Bmatrix}\exp[\mathrm{i}(n\alpha x+m\beta z)]. \quad (3)$$

Substituting (3) into the basic equations (1) and (2) we obtain for the (n, m)th Fourier component (with $\partial/\partial t \equiv 0$)

$$\left\{\frac{1}{Re_p}D^2_{n,m}-\mathrm{i}n\alpha(U(y)-C)D_{n,m}+\mathrm{i}n\alpha\frac{\mathrm{d}^2U}{\mathrm{d}y^2}\right\}\hat{v}_{nm}-\epsilon\sum_{\nu=-\infty}^{\infty}\sum_{\mu=-\infty}^{\infty}N^{\mathrm{OS}}_{(n-\nu),(m-\mu);\nu,\mu}=0, \quad (4)$$

$$\left\{\frac{1}{Re_p}D_{n,m}-\mathrm{i}n\alpha(U(y)-C)\right\}\hat{\eta}_{nm}-\mathrm{i}m\beta\frac{\mathrm{d}U}{\mathrm{d}y}\hat{v}_{nm}-\epsilon\sum_{\nu=-\infty}^{\infty}\sum_{\mu=-\infty}^{\infty}N^{\mathrm{SQ}}_{(n-\nu),(m-\mu);\nu,\mu}=0. \quad (5)$$

Here $D_{n,m} = \mathrm{d}^2/\mathrm{d}y^2-k^2_{nm}$, $k^2_{nm} = (n\alpha)^2+(m\beta)^2$. The linear part of (4) (i.e. $\epsilon \equiv 0$) is the well known Orr–Sommerfeld equation for oblique waves while the linear part of (5) is the vertical vorticity or Squire equation. The remaining parts contain the nonlinear convolution terms which can be written in the form (cf. Ehrenstein & Koch 1989)

$$N^{\mathrm{OS}}_{k,l;\nu,\mu} = \frac{K_1}{k^2_{kl}\,k^2_{\nu\mu}}\hat{\eta}_{kl}\left\{2K_1\frac{\mathrm{d}\hat{\eta}_{\nu\mu}}{\mathrm{d}y}+(k^2_{\nu\mu}+2K_2)\,D_{\nu,\mu}\hat{v}_{\nu\mu}\right\}$$
$$-\frac{1}{k^2_{kl}\,k^2_{\nu\mu}}\frac{\mathrm{d}\hat{v}_{kl}}{\mathrm{d}y}\left\{2K_1K_2\frac{\mathrm{d}\hat{\eta}_{\nu\mu}}{\mathrm{d}y}+[K_2(k^2_{\nu\mu}+K_2)-K_1^2]\,D_{\nu,\mu}\hat{v}_{\nu\mu}\right\}$$
$$+\frac{1}{k^2_{\nu\mu}}\hat{v}_{kl}\left\{(k^2_{\nu\mu}+K_2)\frac{\mathrm{d}}{\mathrm{d}y}(D_{\nu,\mu}\hat{v}_{\nu\mu})+K_1\left[\frac{\mathrm{d}^2\hat{\eta}_{\nu\mu}}{\mathrm{d}y^2}+k^2_{\nu\mu}\hat{\eta}_{\nu\mu}\right]\right\},$$

$$N^{\mathrm{SQ}}_{k,l;\nu,\mu} = -\frac{1}{k^2_{kl}}\left\{K_2\frac{\mathrm{d}\hat{v}_{kl}}{\mathrm{d}y}-K_1\hat{\eta}_{kl}\right\}\hat{\eta}_{\nu\mu}$$
$$+\frac{1}{k^2_{kl}}\left\{K_1D_{k,l}\hat{v}_{kl}+K_2\frac{\mathrm{d}\hat{\eta}_{kl}}{\mathrm{d}y}\right\}\hat{v}_{\nu\mu}+\hat{v}_{kl}\frac{\mathrm{d}\hat{\eta}_{\nu\mu}}{\mathrm{d}y}-\hat{\eta}_{kl}\frac{\mathrm{d}\hat{v}_{\nu\mu}}{\mathrm{d}y},$$

with $K_1 = (\nu l-\mu k)\,\alpha\beta$ and $K_2 = (\nu k\alpha^2+\mu l\beta^2)$. In deriving these equations we made use of the relations

$$\hat{u}_{nm} = \mathrm{i}(n\alpha\,\mathrm{d}\hat{v}_{nm}/\mathrm{d}y-m\beta\hat{\eta}_{nm})/k^2_{nm},$$
$$\hat{w}_{nm} = \mathrm{i}(m\beta\,\mathrm{d}\hat{v}_{nm}/\mathrm{d}y+n\alpha\hat{\eta}_{nm})/k^2_{nm},$$
$$\hat{\xi}_{nm} = \mathrm{i}(n\alpha\,\mathrm{d}\hat{\eta}_{nm}/\mathrm{d}y+m\beta\,\mathrm{d}^2\hat{v}_{nm}/\mathrm{d}y^2)/k^2_{nm}-\mathrm{i}m\beta\hat{v}_{nm},$$
$$\hat{\zeta}_{nm} = \mathrm{i}(m\beta\,\mathrm{d}\hat{\eta}_{nm}/\mathrm{d}y-n\alpha\,\mathrm{d}^2\hat{v}_{nm}/\mathrm{d}y^2)/k^2_{nm}+\mathrm{i}n\alpha\hat{v}_{nm},$$

which can be obtained from the definition of the vorticity vector together with the continuity equation.

Reality of the solution implies

$$\hat{\boldsymbol{v}}_{-n,-m} = \overline{\hat{\boldsymbol{v}}_{n,m}},\quad \hat{\boldsymbol{\omega}}_{-n,-m} = \overline{\hat{\boldsymbol{\omega}}_{n,m}},$$

such that only the modes $n \geqslant 0$ need to be considered (barred quantities denote the complex conjugate). Allowing only standing waves in the spanwise direction one can impose the *reflectional symmetry*

$$\{\tilde{u}(-z),\tilde{v}(-z),\tilde{w}(-z)\} = \{\tilde{u}(+z),\tilde{v}(+z),-\tilde{w}(+z)\}.$$

This way one has to solve only for the modes $n \geqslant 0$, $m \geqslant 0$. These conditions imply that for $n > 0$ and $m = 0$, $\hat{\eta}_{n,0} \equiv 0$ and for $n = 0$ and $m > 0$, $\hat{v}_{0,m}$ (together with $\hat{u}_{0,m}$ and $\hat{\zeta}_{0,m}$) is real and $\hat{\eta}_{0,m}$ (together with $\hat{w}_{0,m}$ and $\hat{\xi}_{0,m}$) is purely imaginary. For $n > 0$ and $m = 0$, (5) is identically satisfied, while for $n = 0$ and $m > 0$, (4) is purely real and (5) is purely imaginary. For $n = 0$ and $m = 0$ both equations (4) and (5) are satisfied identically and one has to use the x-momentum equation together with the constant pressure gradient constraint to obtain

$$\frac{1}{Re_p}\frac{\mathrm{d}^2\hat{u}_{00}}{\mathrm{d}y^2}-\epsilon\sum_{\nu=0}^{\infty}\sum_{\mu=0}^{\infty}N^0_{\nu,\mu} = 0, \tag{6}$$

$$N^0_{\nu,\mu} = -\frac{2(2-\delta_{\nu0}-\delta_{\mu0})}{k^2_{\nu\mu}}\mathrm{Im}\left\{\nu\alpha\frac{\mathrm{d}^2\hat{v}_{\nu\mu}}{\mathrm{d}y^2}\bar{\hat{v}}_{\nu\mu}-\mu\beta\frac{\mathrm{d}}{\mathrm{d}y}(\hat{\eta}_{\nu\mu}\bar{\hat{v}}_{\nu\mu})\right\},$$

where $\delta_{n,m}$ denotes Kronecker's symbol.

The special treatment of the (0,0)-term requires an explicit separation of those convolution terms containing $\hat{u}_{00}$, i.e.

$$\sum_{\nu=-\infty}^{\infty}\sum_{\mu=-\infty}^{\infty} N_{(n-\nu),(m-\mu);\nu,\mu} = N_{n,m;0,0}+N_{0,0;n,m}+\sum_{\nu=-\infty}^{\infty}{}''\sum_{\mu=-\infty}^{\infty}{}'' N_{(n-\nu),(m-\mu);\nu,\mu}.$$

Here Σ'' denotes the sum without the (0,0)-terms and

$$N^{\mathrm{OS}}_{n,m;0,0}+N^{\mathrm{OS}}_{0,0;n,m} = -\mathrm{i}n\alpha\left\{\hat{v}_{n,m}\frac{\mathrm{d}^2\hat{u}_{00}}{\mathrm{d}y^2}+n\alpha\hat{u}_{00}\frac{1}{k^2_{nm}}\left[m\beta\frac{\mathrm{d}\hat{\eta}_{nm}}{\mathrm{d}y}-n\alpha D_{n,m}\hat{v}_{nm}\right]\right\},$$

$$N^{\mathrm{SQ}}_{n,m;0,0}+N^{\mathrm{SQ}}_{0,0;n,m} = \mathrm{i}\left\{n\alpha\hat{u}_{00}\,\hat{\eta}_{nm}+m\beta\frac{\mathrm{d}\hat{u}_{00}}{\mathrm{d}y}\hat{v}_{nm}\right\}.$$

Finally the modal no-slip boundary conditions are

$$(n,m)\neq(0,0):\hat{v}_{nm}(y=\pm1)=\frac{\mathrm{d}\hat{v}_{nm}}{\mathrm{d}y}(y=\pm1)=\hat{\eta}_{nm}(y=\pm1)=0,$$

$$(n,m)=(0,0):\hat{u}_{00}(y=\pm1)=0.$$

A further reduction of the nonlinear system can be achieved by taking into account symmetry properties of the modal equations (4), (5) and (6) as well as their solutions. Denoting the modal equations (4) and (5) with $(n,m)\neq(0,0)$ by F^{OS}_{nm} and F^{SQ}_{nm} respectively, and equations (6) by F_{00}, these equations are functions of the modal solution vector $\boldsymbol{u}=(\hat{u}_{00},\hat{v}_{nm},\hat{\eta}_{nm})$, $(n,m)\neq(0,0)$ and the parameter vector $\boldsymbol{\lambda}=(\alpha,\beta,Re)$. Then we can define a four-element symmetry group Γ consisting of the operators I, S, T and S·T (I is the identity operator) acting on the solution vector and the modal equations as follows:

$$\begin{aligned}
\mathrm{S}\hat{u}_{00}&=\hat{u}_{00}, & \mathrm{S}F_{00}&=F_{00},\\
\mathrm{S}\hat{v}_{nm}&=(-1)^m\hat{v}_{nm}, & \mathrm{S}F^{\mathrm{OS}}_{nm}&=(-1)^mF^{\mathrm{OS}}_{nm},\\
\mathrm{S}\hat{\eta}_{nm}&=(-1)^m\hat{\eta}_{nm}, & \mathrm{S}F^{\mathrm{SQ}}_{nm}&=(-1)^mF^{\mathrm{SQ}}_{nm},\\
\mathrm{T}\hat{u}_{00}(y)&=\hat{u}_{00}(-y), & \mathrm{T}F_{00}(y)&=F_{00}(-y),\\
\mathrm{T}\hat{v}_{nm}(y)&=(-1)^{n+m+1}\hat{v}_{nm}(-y), & \mathrm{T}F^{\mathrm{OS}}_{nm}(y)&=(-1)^{n+m+1}F^{\mathrm{OS}}_{nm}(-y),\\
\mathrm{T}\hat{\eta}_{nm}(y)&=(-1)^{n+m}\hat{\eta}_{nm}(-y), & \mathrm{T}F^{\mathrm{SQ}}_{nm}(y)&=(-1)^{n+m}F^{\mathrm{SQ}}_{nm}(-y).
\end{aligned}$$

Writing the modal equations (4), (5) and (6) formally as

$$\boldsymbol{F}[\boldsymbol{u},\boldsymbol{\lambda}]=0,$$

we showed in Ehrenstein & Koch (1989) that this system is equivariant (i.e. preserved) under the action of the group Γ defined above, i.e.

$$\boldsymbol{F}[\gamma\boldsymbol{u},\boldsymbol{\lambda}]=\gamma\boldsymbol{F}[\boldsymbol{u},\boldsymbol{\lambda}]\quad(\gamma\in\Gamma).$$

The importance of symmetries and the corresponding equivariance properties in bifurcation problems has been emphasized by Golubitsky, Stewart & Schaeffer (1988). The above-stated symmetry properties enable us to consider separately symmetric nonlinear solutions of the form

$$\left.\begin{aligned}
\{\hat{v}^{(\mathrm{s})}_{nm}(-y),\hat{\xi}^{(\mathrm{s})}_{nm}(-y),\hat{\zeta}^{(\mathrm{s})}_{nm}(-y)\}&=(-1)^{n+1}\{\hat{v}^{(\mathrm{s})}_{nm}(+y),\hat{\xi}^{(\mathrm{s})}_{nm}(+y),\hat{\zeta}^{(\mathrm{s})}_{nm}(+y)\},\\
\{\hat{u}^{(\mathrm{s})}_{nm}(-y),\hat{w}^{(\mathrm{s})}_{nm}(-y),\hat{\eta}^{(\mathrm{s})}_{nm}(-y)\}&=(-1)^{n}\{\hat{u}^{(\mathrm{s})}_{nm}(+y),\hat{w}^{(\mathrm{s})}_{nm}(+y),\hat{\eta}^{(\mathrm{s})}_{nm}(+y)\},
\end{aligned}\right\}\quad(7)$$

and antisymmetric nonlinear solutions of the form

$$\left.\begin{aligned}\{\hat{v}^{(\mathrm{a})}_{nm}(-y), \hat{\xi}^{(\mathrm{a})}_{nm}(-y), \hat{\zeta}^{(\mathrm{a})}_{nm}(-y)\} &= (-1)^{n+m+1}\{\hat{v}^{(\mathrm{a})}_{nm}(+y), \hat{\xi}^{(\mathrm{a})}_{nm}(+y), \hat{\zeta}^{(\mathrm{a})}_{nm}(+y)\},\\ \{\hat{u}^{(\mathrm{a})}_{nm}(-y), \hat{w}^{(\mathrm{a})}_{nm}(-y), \hat{\eta}^{(\mathrm{a})}_{nm}(-y)\} &= (-1)^{n+m}\{\hat{u}^{(\mathrm{a})}_{nm}(+y), \hat{w}^{(\mathrm{a})}_{nm}(+y), \hat{\eta}^{(\mathrm{a})}_{nm}(+y)\}.\end{aligned}\right\} \quad (8)$$

The solutions defined by (7) are invariant according to the operator S·T while the solutions defined by (8) are invariant according to T. In our present investigation we do not consider asymmetric nonlinear solutions, being those which do not satisfy (7) or (8). We shall see that the symmetric and antisymmetric linear secondary instability modes discussed by Herbert (1984) are special cases of the above nonlinear solutions for $m = 1$. For the two-dimensional problem, $m \equiv 0$, Herbert (1977) has already demonstrated the existence of symmetric and antisymmetric nonlinear solution branches which reduce to the corresponding symmetric and antisymmetric linear primary instability modes.

By considering only the above-defined symmetric and antisymmetric nonlinear solutions we may limit our computations to the half channel $0 \leqslant y \leqslant 1$ by replacing the no-slip boundary conditions at $y = -1$ by the relevant symmetry conditions at $y = 0$. To fix the amplitude and the phase of the solution we apply in general the local normalization

$$\hat{v}_{10}(y = 0) = 1. \quad (9)$$

Only if $\hat{v}_{10}$ is identically equal to zero, as is the case for the nonlinear three-dimensional primary instability branch, do we use the alternative normalization

$$\hat{v}_{11}(y = 0) = 1.$$

2.3. *Numerical solution procedure*

For the numerical computation the modal expansion (3) is truncated at $n = N$, $m = M$. $\hat{u}_{00}(y)$ as well as each Fourier component $\hat{q}_{nm}(y) \equiv \{\hat{v}_{nm}(y), \hat{\eta}_{nm}(y)\}$, $(n, m) \neq (0, 0)$ is expanded into a Chebyshev series

$$\hat{q}_{nm}(y) = \sum_{k=0}^{2K-1} a_k T_k(y),$$

truncated at $2K-1$ for the full-channel problem. Here $T_k(y) = \cos(k \cos^{-1} y)$ is the kth-order Chebyshev polynomial. If only half the channel is used, the corresponding components are expanded in terms of even and odd Chebyshev polynomials (see Ehrenstein & Koch 1989)

$$\hat{q}_{nm}(y) = \sum_{k=0}^{K-1} a_{2k} T_{2k}(y), \quad \hat{q}_{nm}(y) = \sum_{k=0}^{K-1} a_{2k+1} T_{2k+1}(y),$$

truncated at $K-1$. $\hat{u}_{00}(y)$ as well as each Fourier component $\hat{q}_{nm}(y)$ is then evaluated at the $2K$ (full-channel problem) collocation points $y_j = \cos[j\pi/(2K-1)]$, $j = 0, 1, \dots, 2K-1$. Writing

$$\hat{u}_{00j} = \hat{u}_{00}(y_j); \hat{q}_{nmj} = \hat{q}_{nm}(y_j) \quad (j = 0, 1, \dots, 2K-1), \quad (10)$$

for the unknown functions at the $2K$ collocation points, the pth derivative

$$\hat{q}^{(p)}_{nmj} \equiv \mathrm{d}^p \hat{q}_{nm}(y)/\mathrm{d}y^p|_{y=y_j}$$

can be computed from $\hat{q}_{nmj}$ by means of the collocation matrix method (cf. Gottlieb, Hussaini & Orszag 1984), i.e.

$$\hat{q}^{(p)}_{nmj} = \sum_{k=0}^{2K-1} D^{(p)}_{jk} \hat{q}_{nmk}, \quad (11)$$

with $D^{(p)}_{jk} = (D_{jk})^p$. The derivative matrix D_{jk} has been derived in Gottlieb *et al.* (1984) and the corresponding symmetric and antisymmetric derivative matrices for the half-channel problem with K collocation points are simply

$$D^{(s)}_{jk} = D_{jk} + D_{j,\,2K-1-k},$$

$$D^{(a)}_{jk} = D_{jk} - D_{j,\,2K-1-k}.$$

Instead of replacing suitable rows in the discretization matrix, as suggested by Gottlieb *et al.* (1984), we imposed the boundary conditions by following a method of Ehrenstein (1988) which eliminates spurious (unstable) modes.

Substituting (10) and (11) into the normalization condition (9) as well as into the modal equations (4), (5) and (6), and satisfying the latter at each collocation point, a large system of nonlinear algebraic equations results which is of the form

$$\boldsymbol{F}(\boldsymbol{u};\boldsymbol{\lambda}) = 0. \tag{12}$$

The solution vector $\boldsymbol{u}$ is now defined by

$$\boldsymbol{u} \equiv \{\hat{u}_{00j}; \mathrm{Re}\,(\hat{v}_{nmj}), \mathrm{Im}\,(\hat{v}_{nmj}), \mathrm{Re}\,(\hat{\eta}_{nmj}), \mathrm{Im}\,(\hat{\eta}_{nmj}); C, \epsilon\},$$

with $0 \leqslant n \leqslant N$, $0 \leqslant m \leqslant M$ but $(n,m) \neq (0,0)$ and $0 \leqslant j \leqslant 2K-1$ for the full-channel problem or $0 \leqslant j \leqslant K-1$ for the half-channel problem. Note that the wave speed C is part of the solution vector $\boldsymbol{u}$. $\boldsymbol{\lambda}$ denotes the parameter vector (α, β, Re). Starting with a known solution $\boldsymbol{u}(\boldsymbol{\lambda}_0)$ the nonlinear algebraic system (12) is solved by Newton–Raphson iteration in conjunction with Keller's (1977) pseudo-arclength continuation procedure. At a simple bifurcation point, signalled by a sign change of the Jacobian determinant, a local bifurcation analysis provides the initial estimate for the solution on the bifurcating branch.

In Keller's (1977) pseudo-arclength continuation procedure a parameterizing equation of the form

$$N(\boldsymbol{u},\lambda,s) \equiv \theta(\boldsymbol{u}(s)-\boldsymbol{u}(s_0))\,\mathrm{d}\boldsymbol{u}/\mathrm{d}s(s_0) + (1-\theta)\,(\lambda(s)-\lambda(s_0))\,\mathrm{d}\lambda/\mathrm{d}s(s_0) - (s-s_0) = 0,$$

is added to the system (12). Here s can be thought of as an arclength along the solution curve with s_0 denoting the previously computed point. The tuning factor $0<\theta<1$ allows us to place different emphasis on the solution vector $\boldsymbol{u}$ and the branching parameter λ, keeping all other control parameters fixed. This extended system comprising $\boldsymbol{F}(\boldsymbol{u},\lambda)$ and $N(\boldsymbol{u},\lambda,s)$ avoids the singularity of ordinary parameter continuation at a turning (limit) point of the solution curve.

2.4. *Quantities of physical interest*

The amplitude ϵ is defined once we specify the normalization condition (9). However, instead of ϵ it is customary to use as a scalar measure of nonlinearity the total fluctuation energy E of the harmonic modes, normalized with the energy of the laminar flow $U(y)$, i.e.

$$E = \sum_{\substack{n=0 \\ (n,m)\neq(0,0)}}^{N} \sum_{m=0}^{M} E_{n,m}; \quad E_{n,m} = \frac{15\epsilon^2}{4(1+\delta_{n0})\,(1+\delta_{m0})} \int_{-1}^{1} [\hat{\boldsymbol{v}}_{nm}(y)\cdot\overline{\hat{\boldsymbol{v}}_{nm}}(y)]\,\mathrm{d}y.$$

In order to compare our constant pressure gradient solution with experimental results we need to know Re_Q, or better $Re_{Q_m} = U^*_m h^*/\nu^*$ the Reynolds number defined with the average velocity U^*_{m} across the channel. This average velocity can easily be found by integrating the mean velocity profile $u_{\mathrm{m}}(y)$

$$u_{\mathrm{m}}(y) = U(y) + \epsilon \hat{u}_{00}(y),$$

which at the same time gives an indication of the deviation from the parabolic laminar profile $U(y)$. For laminar flow $Re_p = Re_Q = \frac{3}{2} Re_{Q_{\mathrm{m}}}$.

Of prime importance for engineering applications is the local friction factor c_{f} which is generally defined as the ratio of the mean wall shear stress to the dynamic head of the flow, i.e.

$$c_{\mathrm{f}} = \frac{\mu^*(\partial u^*_{\mathrm{m}}/\partial y^*)_{y^*=-h^*}}{\frac{1}{2}\rho^* U^{*2}_{\mathrm{m}}}.$$

In channel flow the mean wall shear stress can be related to the average pressure gradient (cf. Schlichting 1958),

$$-\frac{\mathrm{d}p^*}{\mathrm{d}x^*} = \frac{c_{\mathrm{f}}}{h^*}\frac{\rho^* U^{*2}_{\mathrm{m}}}{2}.$$

With $\mathrm{d}p^*/\mathrm{d}x^*$ being constant and equal to the laminar pressure gradient, one finds

$$c_{\mathrm{f}} = 9 Re_p / Re_Q^2,$$

which for laminar flow reduces to $c_{\mathrm{f}} = 9/Re_p = 9/Re_Q = 6/Re_{Q_{\mathrm{m}}}$.

3. Wavelike primary bifurcation solutions

To start the pseudo-arclength continuation procedure we need a known solution. In general this known solution is a wave-like primary bifurcation solution which originates from the steady laminar solution via Hopf bifurcation. In this section we review briefly the linear and nonlinear primary bifurcation stage and extend the nonlinear equilibrium solutions to three dimensions allowing a comparison with Dhanak's (1983) weakly nonlinear three-dimensional theory. To help the reader distinguish the various solution branches figure 2 displays the corresponding modal patterns in the (n, m) Fourier plane. At the same time the main truncations used in the present paper are indicated by the cross-hatched area.

3.1. *Neutral three-dimensional linear disturbances*

The linear, neutral primary instability surface of plane Poiseuille flow, depicted in figure 3, is a well-known result of classical hydrodynamic stability theory (see Drazin & Reid 1981) and corresponds to the modal pattern (*a*) or (*b*) in figure 2. It is obtained by solving (4) and (5) linearized about $\epsilon = 0$ with $n = m = 1$ and real α, β and C. The spectrum of the corresponding eigenvalue problem is known to be discrete and complete and at most one symmetric (wall) eigenmode can become unstable. Orszag (1971) computed the critical condition as $Re_{\mathrm{crit}} = 5772.22$, $\alpha_{\mathrm{crit}} = 1.02056$ and $C_{\mathrm{crit}} = 0.26400174$ which according to Squire's (1933) theorem is two dimensional. The linear neutral surface of figure 3 is the starting point for nonlinear (super-) harmonic bifurcation solutions. Craik's subharmonic triad resonance is also possible on this neutral surface, namely for $Re = 11664$, $\alpha = 1.0881$, $\beta = 0.709$ and $C = 0.2391$. Starting from this symmetric triad, Shtern (1976) computed the bifurcation curves on the linear neutral surface for general triad resonances which are also depicted in figure 3 together with their projections. However, owing to symmetry arguments,

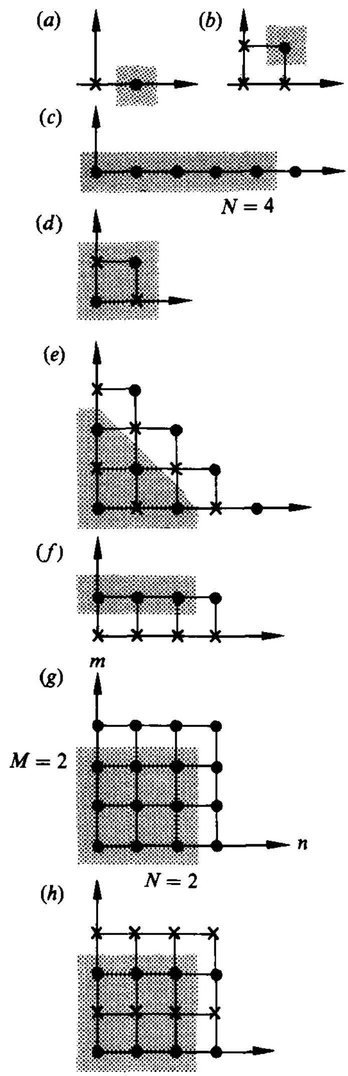

FIGURE 2. Modal pattern (n, m) of various solutions; ●, modes excited, ×, modes not excited. Shaded area marks modal truncation used in present paper. (*a*), (*b*) Two-dimensional or three-dimensional linearized primary bifurcation solution. (*c*) Two-dimensional primary bifurcation solution. (*d*) Three-dimensional mean field solution. (*e*) Three-dimensional primary bifurcation solution. (*f*) Three-dimensional linearized secondary bifurcation solution. (*g*) Three-dimensional secondary bifurcation solution $M^{(n,m)}$. (*h*) Three-dimensional secondary bifurcation solution $M^{(n,2m)}$.

Craik's subharmonic triad mechanism is usually regarded as inactive in plane Poiseuille flow (see for example Herbert 1988) and will not be pursued in this paper.

3.2. *Neutral two-dimensional nonlinear disturbances*

With Re_{crit} attained for two-dimensional disturbances, historically two-dimensional nonlinear extensions of the neutral surface, corresponding to the modal pattern (*c*) in figure 2, have been investigated first. Setting $\beta \equiv 0$ the total fluctuation energy E is usually taken as a measure of nonlinearity. This pulsation energy surface for the frequently cited example with $N = 2, M = 0$, see Zahn *et al.* (1974) or Herbert (1977),

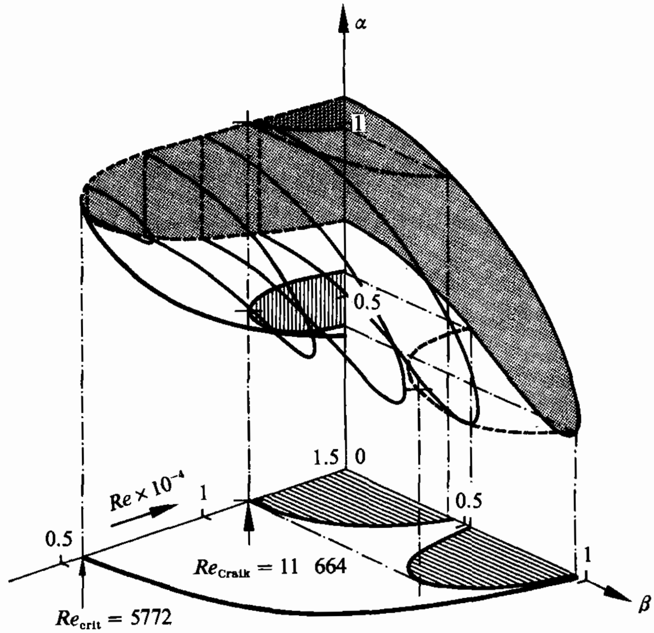

FIGURE 3. Perspective view of three-dimensional linear neutral surface, with ----, subharmonic bifurcation curves starting at Craik's triad resonance.

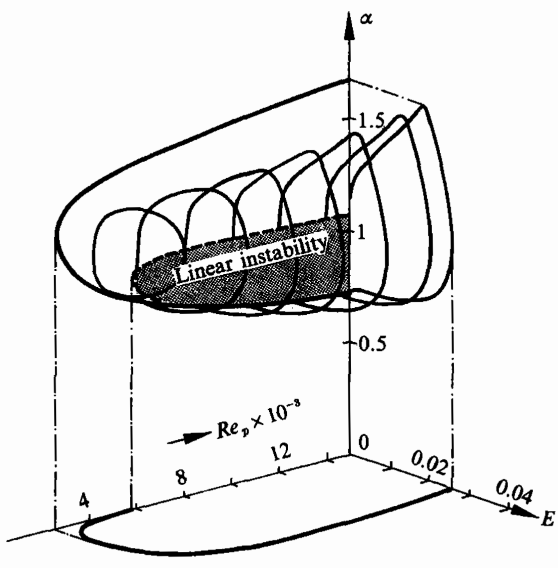

FIGURE 4. Perspective view and projections of two-dimensional ($\beta = 0$) nonlinear equilibrium surface E (Re_p, α) with $K = 20$ and $N = 2$.

is depicted in figure 4. Various $Re_p =$ constant cuts are shown as well as the projections of the two-dimensional surface, clearly indicating the strong reduction of Re_{crit}. The $N = 2$ solution is already in qualitative agreement with the results of two-dimensional weakly nonlinear theories (cf. Pekeris & Shkoller 1969 or Chen & Joseph 1973), i.e. the upper linear branch including Re_{crit} is subcritically unstable with a finite threshold amplitude while most of the lower branch (for $Re_p >$ about 7500) is

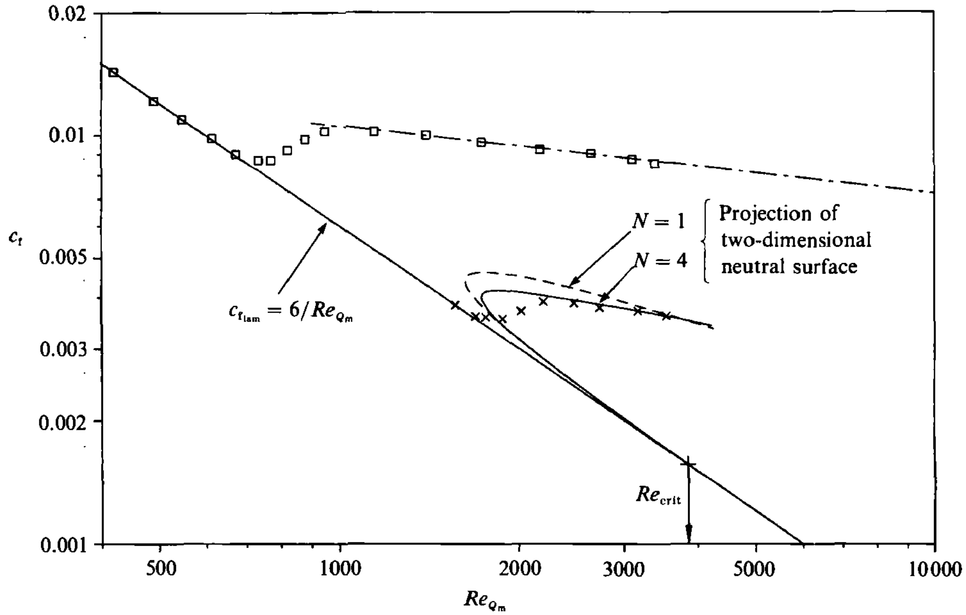

FIGURE 5. Friction factor c_f of the projected two-dimensional equilibrium surface as a function of Re_{Q_m} for $K = 20$ and $N = 1$ and $N = 4$. $\times$, two-dimensional simulation of Rozhdestvensky & Simakin (1984) with $N = 4$, $\square$, Patel & Head's (1969) experiment.

supercritically unstable with a bounded equilibrium solution. However, quantitative changes for higher truncations, especially at higher Reynolds numbers, see Milinazzo & Saffman (1985) or Ehrenstein & Koch (1989), indicate that the $N = 2$ solution has not fully converged yet.

The projection of the two-dimensional neutral surface is shown in figure 5 and figure 6 for $N = 1$ and $N = 4$ in relation to experimental and two-dimensional numerical simulation results. The $N = 4$ numerical simulation results of Rozhdestvensky & Simakin (1984) for the projection of the two-dimensional equilibrium surface (their 'limiting' flow) as well as the $\alpha = 1.25$ cut in figure 6 agree quite well with our $N = 4$ bifurcation results. The deviations at lower Reynolds numbers are apparently due to the fact that for these low Reynolds numbers Rozhdestvensky & Simakin (1984) could only find equilibrium solutions for long-wavelength disturbances. These correspond to quasi-periodic flows with two or more characteristic lengthscales in contrast to our periodic solutions.

At first sight this good agreement is surprising because in general the simulation will not converge to a periodic solution. However, investigating the stability of the above two-dimensional finite-amplitude flow to infinitesimal two-dimensional superharmonic disturbances, Pugh & Saffman (1988) found that the upper branch becomes stable to constant-pressure gradient disturbances for larger Reynolds numbers. At lower Reynolds numbers they discovered a subcritical Hopf bifurcation in the moving frame possibly leading to stable quasi-periodic flows at low Reynolds numbers which would explain Rozhdestvensky & Simakin's (1984) long-wavelength simulation results. These findings are in general agreement with the two-dimensional time-dependent numerical simulations of Jiménez (1987*b*, 1990), who not only found quasi-periodic flows but also evidence of chaos. Jiménez relates the new solutions to a bursting phenomenon in the sublayer near the wall which could coexist with three-dimensional instabilities in the core of the flow.

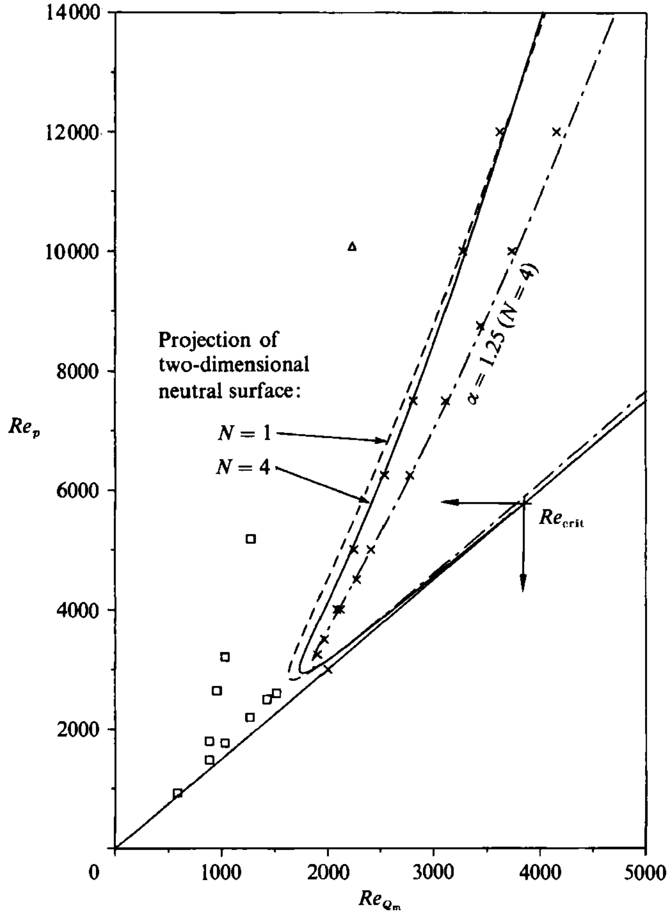

FIGURE 6. Re_p *vs.* Re_{Q_m} for projected two-dimensional equilibrium surface with $K = 20$, $N = 1$ and $N = 4$. $\times$, two-dimensional simulation of Rozhdestvensky & Simakin (1984) for $N = 4$, $\square$, Tillmann's experiment, see Herbert (1977), $\triangle$, Eckelmann's (1970) experiment. Also shown is a cut for $\alpha = 1.25$ with $K = 20$, $N = 4$ compared to Rozhdestvensky & Simakin's (1984) two-dimensional simulation results for $N = 4$.

To give a general idea of the nonlinear two-dimensional equilibrium solution the disturbance streamlines of the two-dimensional lower and upper equilibrium branch in the moving system are plotted in figure 7 for the often cited example $Re_p = 5000$ and $\alpha = 1.12$.

3.3. *Neutral three-dimensional nonlinear disturbances*

With the experimental findings in mind that two-dimensional disturbances soon become three-dimensional in transitional flow, it is only natural to investigate three-dimensional equilibrium solutions which bifurcate off the linear neutral surface depicted in figure 3. The resulting equilibrium surface for three-dimensional disturbances is four-dimensional, i.e. (Re, α, β, E), and it is customary to display the solution in cut planes keeping two of the parameters fixed. Using the mean-field approach, which allows nonlinear interaction only between the (0, 0) and the (1, 1) mode (cf. modal pattern (*d*) in figure 2), Grohne (1969) and Zahn *et al.* (1974) have already published extensions to nonlinear three-dimensional disturbances. They

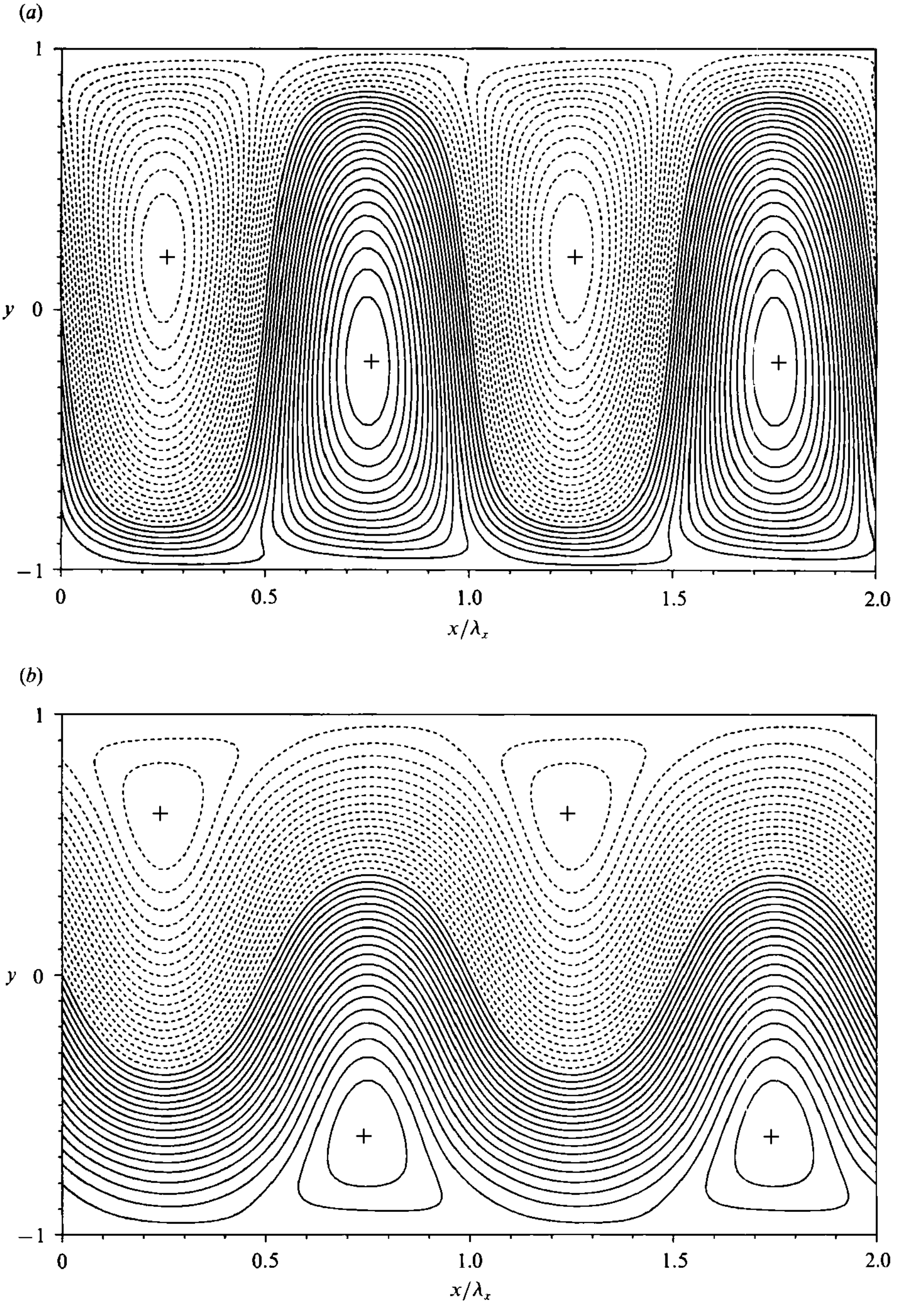

FIGURE 7. Disturbance streamlines ($\Delta\psi = \frac{1}{40}[\psi_{max} - \psi_{min}]$) of two-dimensional equilibrium surface in the moving system for $Re_p = 5000$, $\alpha = 1.12$ with $K = 15$ and $N = 2$. (*a*) lower branch, $C = 0.2878$, (*b*) upper branch, $C = 0.3069$.

observed that these solutions do not lead to a reduced critical Reynolds number and that three-dimensionality has a strong stabilization effect. These results were confirmed by Koch (1988) but disagree qualitatively with the weakly nonlinear results of Dhanak (1983).

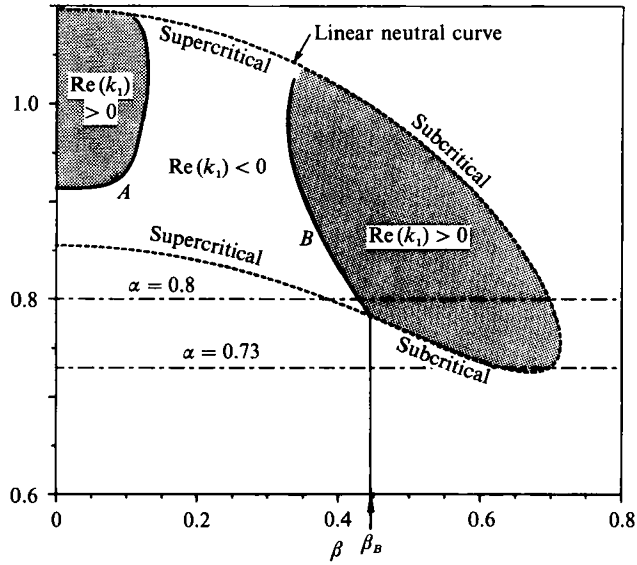

FIGURE 8. Regions of sub- and supercriticality near three-dimensional neutral curve for $Re = 8000$ (adapted from Dhanak 1983).

Dhanak (1983) investigated the small-amplitude behaviour of three-dimensional disturbances forming standing waves in a spanwise direction by expanding about the linear neutral surface. Numerically computing the (Landau) coefficient k_1, Dhanak (1983) identified the regions of subcritical and supercritical equilibrium solutions in the (α, β)-plane for $Re \leqslant 8000$. Here the term *subcritical* is used in the sense that the nonlinear solution, starting on the linear neutral curve extends into the linearly stable region implying the existence of a finite threshold amplitude before the nonlinear solution becomes unstable. On the other hand, a nonlinear solution is termed *supercritical* if it continues into the linearly unstable region forming a (locally stable) finite equilibrium state. Dhanak's main finding is that the real part of k_1 can vanish along two separate curves in the (α, β)-plane, denoted branch A and B by Dhanak (compare figure 8 which has been adapted from Dhanak's (1983) figure 4). For our chosen example with $Re = 8000$ this means that along the lower branch of the linear neutral curve with $\beta < \beta_B$ the nonlinear solution is supercritical, while for $\beta > \beta_B$ it is subcritical.

Figure 9 shows the low-amplitude behaviour of Koch's (1988) strongly nonlinear results for a modal truncation $N = M = 1$, $Re_p = 8000$ and various $\alpha =$ constant cuts. Only the (1, 1) and (0, 0) modes are excited, which explains the agreement with Zahn *et al.*'s (1974) mean-field solution. Selecting the $\alpha = 0.8$ cut we see that our $N = M = 1$ result displays a threshold amplitude for $\beta < \beta_B$ of figure 8 and a finite-amplitude equilibrium for $\beta > \beta_B$. This is just the opposite of Dhanak's (1983) prediction. A similar discrepancy between the weakly nonlinear prediction and the $N = 1$ Fourier truncation for two-dimensional solutions could be corrected by going to higher Fourier truncations. Therefore we consider next the truncation $N = M = 2$.

In this case only the (0, 0), (0, 2), (1, 1), (2, 0) and (2, 2) modes are excited forming a chess-board-like modal pattern. This modal pattern is similar to the one for subharmonic transition observed by May & Kleiser (1985) in their time-dependent simulation. And indeed, this solution branch contains the superharmonic resonant triad $(2\alpha, 0)$ and $(\alpha, \pm\beta)$ on the linear neutral surface with $\alpha = 0.5506$, $\beta = 0.709$ and

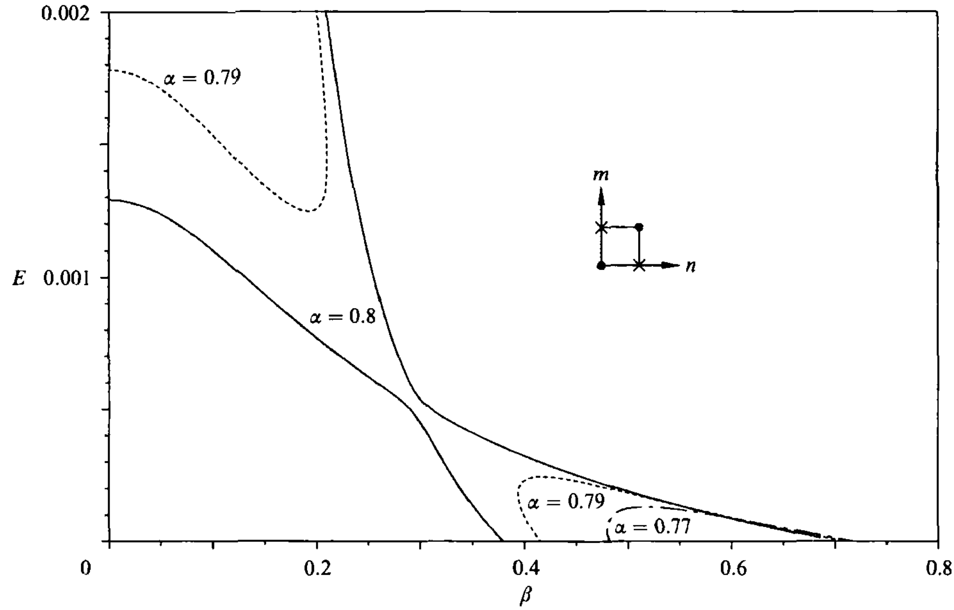

FIGURE 9. Small-amplitude behaviour of three-dimensional primary equilibrium surface $E(\beta)$ for $Re_p = 8000$ and various α = constant cuts with $K = 15$ and $N = M = 1$.

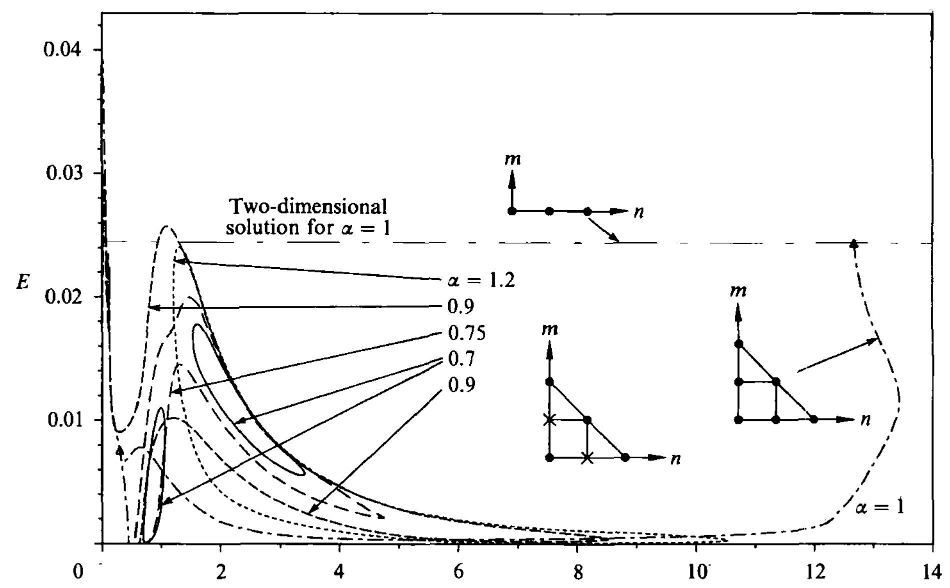

FIGURE 10. Three-dimensional primary equilibrium surface $E(\beta)$ for $Re_p = 8000$ and various α = constant cuts with $K = 15$ and triangular modal cut off at $N = M = 2$.

$Re = 11664$. Goldshtik, Lifshits & Shtern (1983) have investigated this triad and disappointingly found results similar to the nonlinear two-dimensional branch. In this superharmonic solution branch the (0, 2) mode appears to dominate while the energy in the (2, 2) mode is negligibly small in most cases. Therefore, in order to save computer time, all following parameter studies for this three-dimensional solution

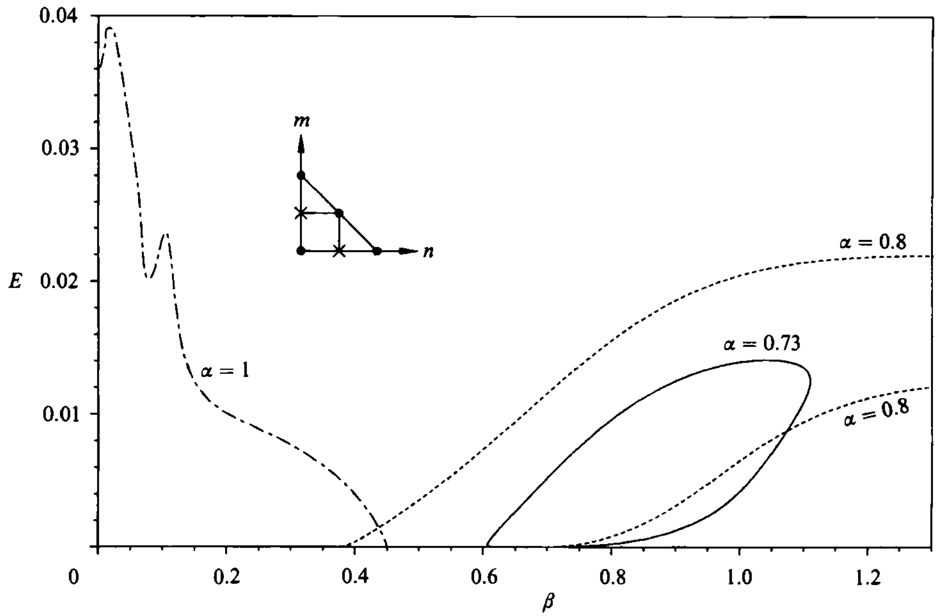

FIGURE 11. Small-β behaviour of three-dimensional primary equilibrium surface $E(\beta)$ of figure 10 with $K = 15$ and triangular modal cut off at $N = M = 2$.

branch have been performed by using a triangular modal cut off, i.e. for $N = M = 2$ only the modes (0, 0), (0, 1), (0, 2), (1,0), (1, 1) and (2, 0) have been retained, corresponding to modal pattern (*e*) in figure 2. The results of this computation are shown in figure 10 with an enlargement of the low β region depicted in figure 11.

Selecting again the $\alpha = 0.8$ cut in figure 11 we see that we have now a finite-amplitude equilibrium for $\beta < \beta_B$ and a threshold amplitude for $\beta > \beta_B$ in agreement with Dhanak's (1983) small-amplitude predictions. For the $\alpha = 0.73$ cut we observe a threshold amplitude on both sides of the neutral curve (even though Dhanak did not continue his curve B, cf. figure 8, down to $\alpha = 0.73$ it looks like the $\alpha = 0.73$ is completely to the right of curve B). As can be seen from figure 10 the global $N = M = 2$ results, covering a wide range in the β domain, differ completely from the $N = M = 1$ result of Koch (1988), an indication that probably several more modes should be retained for quantitatively correct values. This is not being pursued in this investigation because the disturbance energies and friction factors of this solution class are comparable to those of the nonlinear two-dimensional solution. Similar to the nonlinear two-dimensional solution this nonlinear three-dimensional solution serves only as a staging ground for secondary bifurcations, one of which is included in figure 10 for $\alpha = 1$ with the bifurcation points marked by triangles. This secondary bifurcation branch connects the nonlinear three-dimensional primary equilibrium surface of this section with the two-dimensional primary equilibrium surface of §3.2.

From numerical simulations and experimental investigations it became apparent that secondary instabilities play an important role in the transition process. Therefore we shall concentrate in the following on secondary bifurcations and nonlinear equilibrium solutions resulting from these.

4. Wavelike secondary bifurcation solutions

The discovery of Orszag & Patera (1980) and Herbert (1981) that the exponential growth of small three-dimensional disturbances, observed in time-dependent numerical simulations as well as shear-flow experiments, can be explained by a linear secondary instability, cf. modal pattern (f) in figure 2, of the finite-amplitude two-dimensional equilibrium branch constituted a major breakthrough in theoretical transition research. The neutral states of these secondary instabilities are the bifurcation points for our nonlinear secondary bifurcation branches. Therefore we present at first a brief review of the linear secondary instability results for plane Poiseuille flow.

4.1. *Secondary instabilities*

The periodicity of the nonlinear primary equilibrium state allows the application of Floquet or Bloch theory (cf. Herbert 1988), to compute the growth rate of secondary instabilities using similar numerical methods as for linear primary instability. Investigating two-dimensional secondary disturbances Pugh (1987) and Pugh & Saffman (1988) found a much richer picture of possible instabilities than the simple stability transition hitherto assumed to hold at the nose of the two-dimensional nonlinear equilibrium surface. However, for our investigation three-dimensional secondary disturbances are of prime interest and corresponding numerical results have been published for the lower two-dimensional branch by Herbert (1981, 1984) and for the upper two-dimensional branch by Orszag & Patera (1980, 1983). Pugh (1987) and Ehrenstein & Koch (1989) gave results for both branches. In particular, Herbert (1984) has demonstrated that for plane Poiseuille flow the (super-) harmonic secondary disturbances can be separated into *symmetric*

$$\{\hat{v}_n^{(s)}(-y), \hat{\xi}_n^{(s)}(-y), \hat{\zeta}_n^{(s)}(-y)\} = (-1)^{n+1}\{\hat{v}_n^{(s)}(+y), \hat{\xi}_n^{(s)}(+y), \hat{\zeta}_n^{(s)}(+y)\},$$
$$\{\hat{u}_n^{(s)}(-y), \hat{w}_n^{(s)}(-y), \hat{\eta}_n^{(s)}(-y)\} = (-1)^{n}\{\hat{u}_n^{(s)}(+y), \hat{w}_n^{(s)}(+y), \hat{\eta}_n^{(s)}(+y)\},$$

and *antisymmetric* contributions

$$\{\hat{v}_n^{(a)}(-y), \hat{\xi}_n^{(a)}(-y), \hat{\zeta}_n^{(a)}(-y)\} = (-1)^{n}\{\hat{v}_n^{(a)}(+y), \hat{\xi}_n^{(a)}(+y), \hat{\zeta}_n^{(a)}(+y)\},$$
$$\{\hat{u}_n^{(a)}(-y), \hat{w}_n^{(a)}(-y), \hat{\eta}_n^{(a)}(-y)\} = (-1)^{n+1}\{\hat{u}_n^{(a)}(+y), \hat{w}_n^{(a)}(+y), \hat{\eta}_n^{(a)}(+y)\}.$$

In the following we consider only (super-) harmonic secondary disturbances and most results to be presented will be for the frequently used linearly stable test case $Re_p = 5000$ and $\alpha = 1.12$ (cf. Herbert 1984).

Figure 12 depicts the temporal amplification rate $\mathrm{Re}(\sigma)$ of the symmetric secondary instability modes on the lower (a) and upper (b) two-dimensional equilibrium branch as a function of spanwise wavenumber β for $N = 1$ and $K = 20$ collocation points in the half channel. On the lower branch the most unstable secondary instability mode, shown by a solid line, is phase locked with the two-dimensional wave, i.e. $\mathrm{Im}(\sigma_1) = 0$ in the system moving with C_{2D}. Non-phase-locked modes represent quasi-periodic solutions and are depicted by dashed lines. For some parameters (in particular larger spanwise wavenumbers β) the amplification rate of the non-phase-locked modes is much higher than that of the phase-locked modes. Despite this, we only include phase-locked modes in the present paper because the physical importance of the non-phase-locked modes needs further clarification. The detailed growth rates for small β are shown enlarged in the inserts of figure 12. In particular the behaviour on the upper branch, where a pair of complex conjugate non-phase-locked instability modes splits into two unstable phase-locked modes is

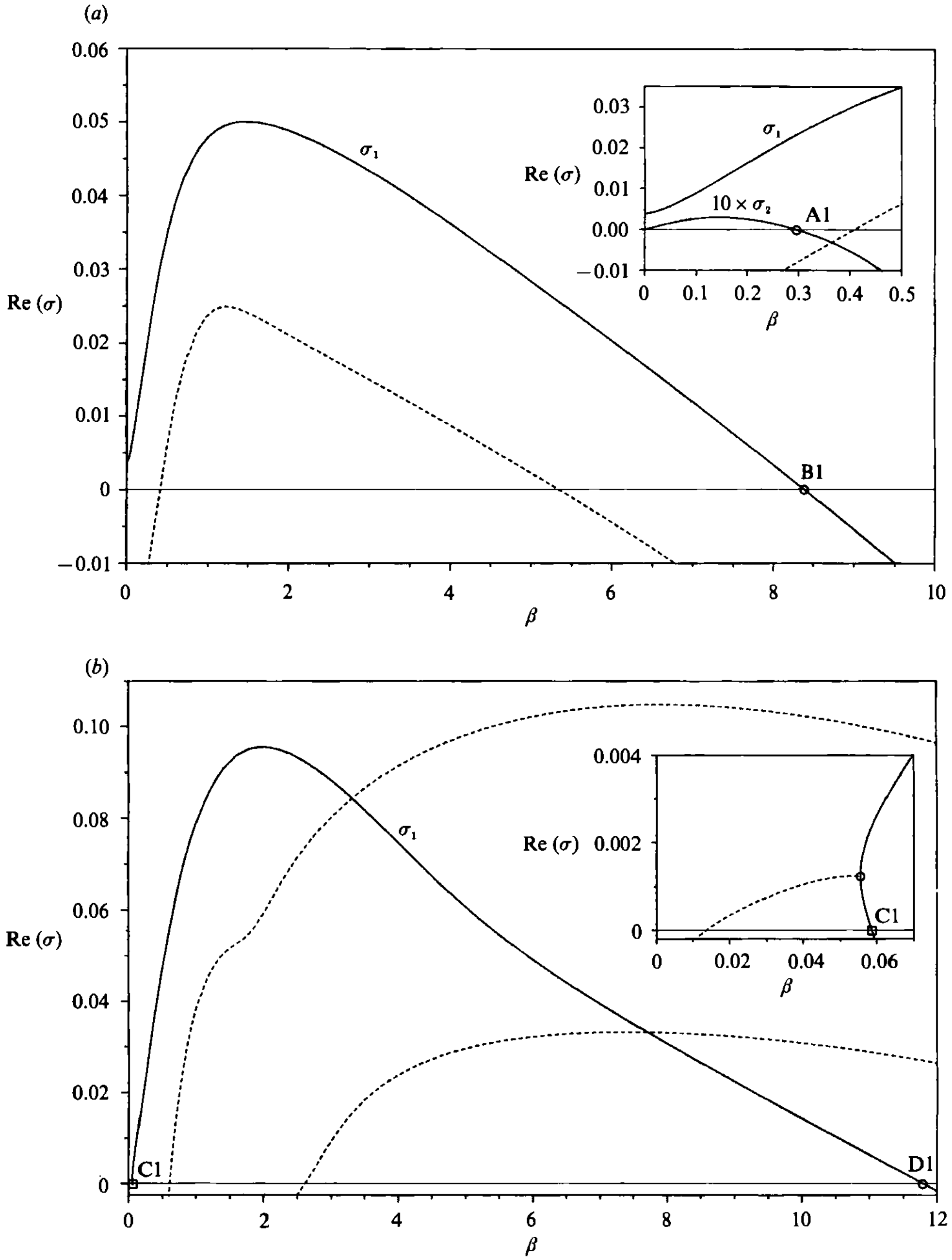

FIGURE 12. Temporal amplification rate $\mathrm{Re}(\sigma)$ of symmetric secondary instability modes on the lower (a) and upper (b) two-dimensional equilibrium branch for $Re_p = 5000$, $\alpha = 1.12$, $K = 20$ and $N = 1$.

interesting and analogous to a similar phenomenon observed by Pugh & Saffmann (1988) for two-dimensional disturbances. However, in this paper we are mainly interested in the points where the phase-locked modes become neutral, i.e. points A1 and B1 on the lower two-dimensional branch or points C1 and D1 on the upper two-dimensional branch.

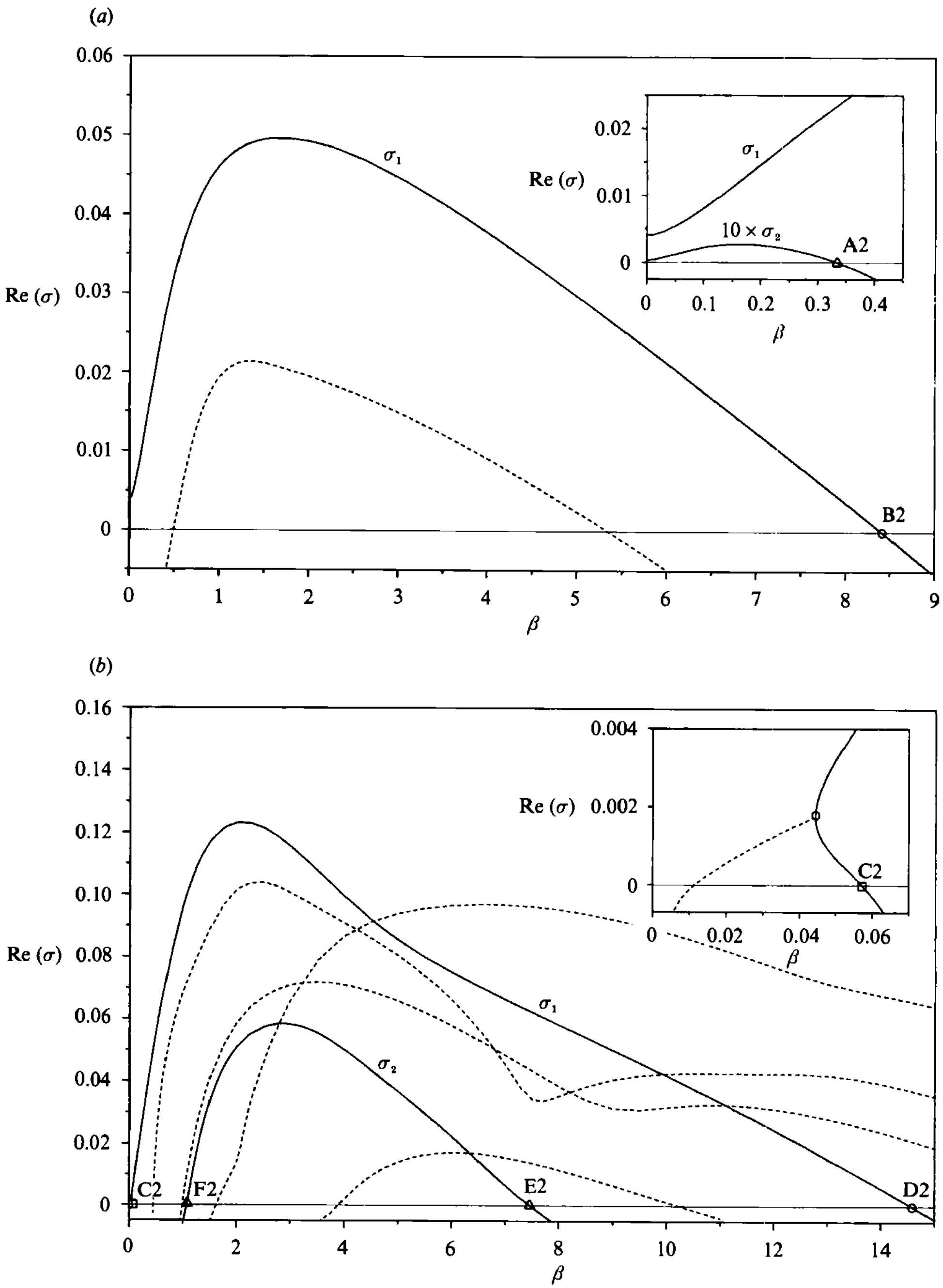

FIGURE 13. Temporal amplification rate $\mathrm{Re}(\sigma)$ of symmetric secondary instability modes on the lower (a) and upper (b) two-dimensional equilibrium branch for $Re_p = 5000$, $\alpha = 1.12$, $K = 20$ and $N = 2$.

Increasing the truncation to $N = 2$ we obtain the situation shown in figure 13. While the behaviour on the lower branch is similar to the one for $N = 1$ we notice important qualitative changes on the upper branch for $N = 2$: several additional unstable modes appear and of particular interest is a second unstable phase-locked mode σ_2 with neutral points at E2 and F2. The antisymmetric secondary instability modes, not displayed here, show similar behaviour, with the exception that the phase-locked modes σ_1 and σ_2 are interconnected on the upper branch for the parameters chosen.

Orszag & Patera (1983) noted that positive secondary-instability growth rates exist for all combinations of Re and α on the upper two-dimensional branch and even below the corresponding nonlinear critical Reynolds number. To make such assertions about secondary instabilities for Reynolds numbers below $Re_{\mathrm{crit}_{2\mathrm{D}}}$ they used what they termed two-dimensional quasi equilibria in conjunction with a shape assumption. This rather heuristic procedure rests upon the hypothesis that these two-dimensional quasi-equilibrium states evolve rather quickly after which the flow decays slowly through viscous relaxation (cf. Bayly *et al.* 1988). Choosing the quasi equilibria to have the same form as the exact two-dimensional equilibrium wave on the upper branch at $Re_p = 4000$ and $\alpha = 1.25$ but with a different amplitude factor $\epsilon_{\mathrm{shape}}$ they computed contours of equal growth rate of secondary instabilities as a function of Reynolds number and two-dimensional quasi-equilibrium wave amplitude. This way they obtained an approximate threshold Reynolds number in the vicinity of 500. This remarkable result stimulated us to investigate the exact three-dimensional secondary bifurcation branches to be discussed in the next section.

To allow a certain qualitative comparison with the following exact results, we also applied the above-described approximate method in figure 14. However, we chose as reference solution for ϵ_{equ} the exact two-dimensional equilibrium waveform on the upper branch of our test case $Re_p = 5000$ and $\alpha = 1.12$. Figure 14 shows equal secondary amplification contours for variable $\epsilon_{\mathrm{shape}}$ and (*a*) variable Re_p with fixed $\beta = 2$ and (*b*) variable β with fixed $Re_p = 5000$. The zero growth-rate curve $\mathrm{Re}(\sigma) = 0$ was expected to give an approximate picture of the exact secondary equilibrium surface for symmetric phase-locked modes to be computed in the next section. The approximate character of the solution in figure 14 can already be seen from the fact that the $\mathrm{Re}(\sigma) = 0$ curve does not pass through the neutral point B1 on the lower two-dimensional branch. For comparison the exact nonlinear two-dimensional domain is shown shaded in figure 14(*a*) indicating that secondary bifurcation branches might lead to much lower critical Reynolds numbers. The rather unusual lobed form of the neutral curve $\mathrm{Re}(\sigma) = 0$ in figure 14(*b*) is due to the appearance of the second unstable phase-locked mode σ_2.

4.2. *Wave-like secondary bifurcation solutions*

In this section we shall investigate mainly symmetric wave-like secondary bifurcation solutions which constitute the most important results of this investigation. These solutions bifurcate at the neutral points of phase-locked secondary instability modes on the nonlinear primary bifurcation surface. Although secondary bifurcations exist on the nonlinear three-dimensional equilibrium surface of §3.3 (see for example the branch for $\alpha = 1$ bifurcating at the points marked by triangles in figure 10) we shall concentrate on those solutions which bifurcate from the nonlinear two-dimensional primary equilibrium surface, because the corresponding bifurcation points can be computed easily via linear secondary instability theory. We shall limit ourselves to the discussion of symmetric and antisymmetric secondary bifurcation branches, defined by (7) and (8) in the half-channel. Asymmetric secondary bifurcation solutions, as well as interactions between these solutions, require computations in the whole channel (cf. the example for $N = M = 1$ presented in Ehrenstein & Koch 1989) and are excluded here.

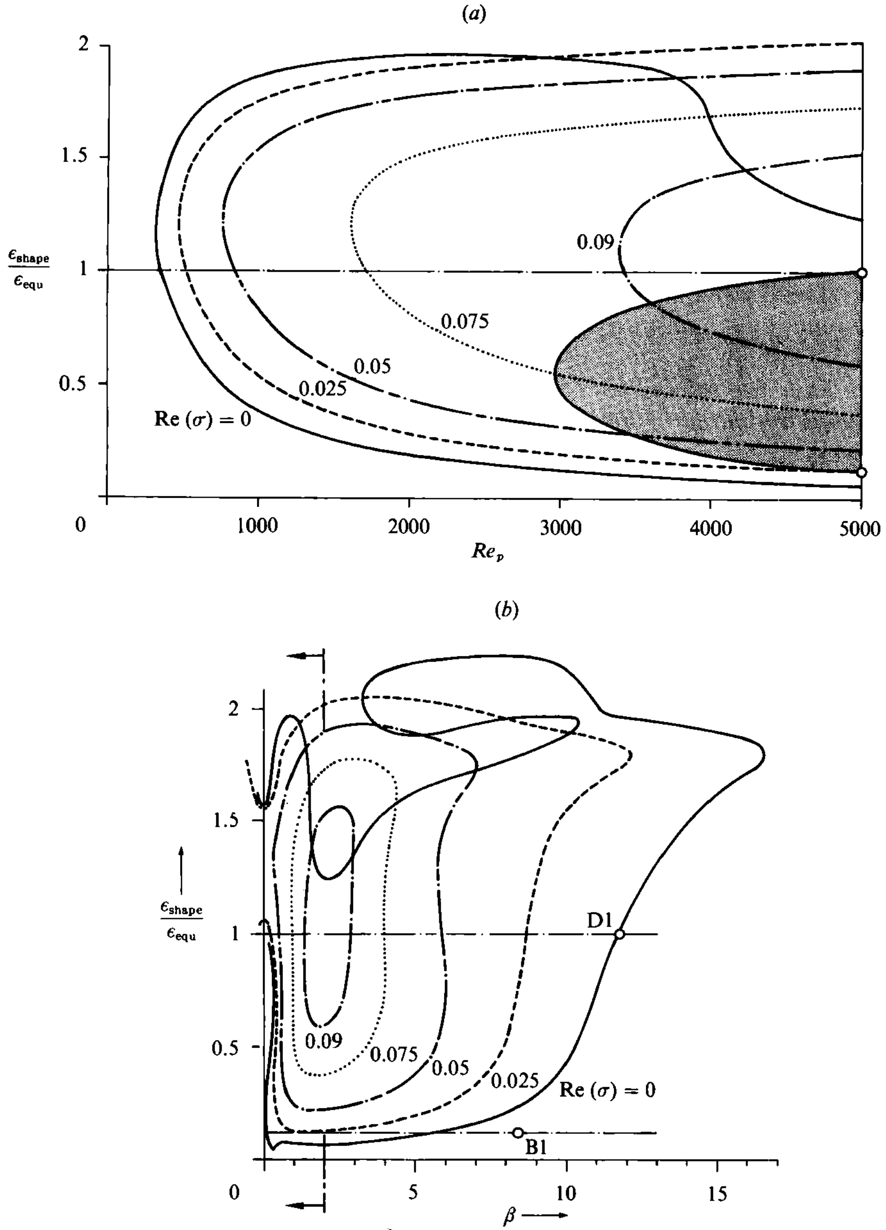

FIGURE 14. Contours of equal (symmetric) secondary instability growth rate Re (σ) on quasi-equilibrium waves for $\alpha = 1.12$, $K = 20$ and $N = 1$ as function of wave amplitude and (*a*) Reynolds number Re_p with fixed $\beta = 2$ and (*b*) spanwise wavenumber β with fixed $Re_p = 5000$.

The secondary instability computations of the previous section indicate that point D2 of figure 13 is a bifurcation point for symmetric and antisymmetric modes. In Ehrenstein & Koch (1989, 1991) we performed a local bifurcation analysis of the whole-channel problem near this bicritical point D2. We showed that the symmetric and antisymmetric solution branches do not interact locally, lending some justification to our separate treatment of symmetric and antisymmetric solution branches. This fact is a consequence of the symmetry properties of the nonlinear system stated in §2. Owing to the existence of multiple or disconnected solution branches the following results are to be considered only as first examples to help understand the rather intricate bifurcation structure. No claim for completeness is made and perhaps other more important branches still exist.

Even with our symmetry assumptions there is a multitude of phase-locked bifurcation points, as is evident from figure 13. In the present paper we limit our results mainly to two families of secondary bifurcation branches. The first family produces what we term $M^{(n,m)}$ branches and contains all Fourier modes represented by the modal pattern (*g*) of figure 2. In the second family, termed $M^{(n,2m)}$ and described by modal pattern (*h*) in figure 2, only even spanwise harmonics are excited. The $M^{(n,2m)}$ branches therefore constitute a spanwise superharmonic solution. To display the main properties of these branches we chose E, β cuts for our model example $Re_p = 5000$ and $\alpha = 1.12$. This example corresponds to the one used in figure 14(*b*) and clearly reveals the relation of the bifurcation points to the zero amplification points in figure 13. Practically all calculations have been performed using the truncation $N = M = 2$.

4.2.1. *Secondary bifurcation solutions* $M^{(n,m)}$ *containing all Fourier modes*

The bifurcation points of the $M^{(n,m)}$ solutions, cf. modal pattern (*g*) of figure 2, are simply the points of zero secondary amplification rate on the nonlinear two-dimensional equilibrium surface as investigated in §4.1. In particular, we concentrate on the points B and D of figures 12 and 13 which are also marked in figure 14(*b*). For our linearly stable subcritical model example $Re_p = 5000$, $\alpha = 1.12$ the corresponding exact global bifurcation results are shown in figure 15 for various truncations. (The results for $Re_p = 8000$ and $\alpha = 1$ in figure 10 give an idea of what the global $M^{(n,m)}$ branch looks like for a linearly unstable case. In this particular example the three-dimensional solution bifurcating from the two-dimensional upper branch ends on the three-dimensional equilibrium surface of §3.3 instead of the two-dimensional lower branch as in the subcritical case).

From figure 15 we see that the fluctuation energy E of the exact bifurcation result reaches a maximum at the two-dimensional upper branch point D and a minimum at the lower branch point B, which is at variance with the approximate result of figure 14. A local analysis shows (cf. Ehrenstein & Koch 1989, 1991) that both bifurcation points correspond to pitchfork bifurcations such that the three-dimensional branches are actually covered twice which does not show in the projection of figure 15. From figure 15 we see also that in agreement with the local results, the solution truncated at $N = M = 1$ is qualitatively different from the solution with higher truncation, i.e. the $N = M = 1$ branch bifurcates to higher values of β while the higher truncations bifurcate to lower values of β. The $N = M = 2$ solution seems to be already fairly close to the $N = M = 3$ solution and we notice again that at least $N = M = 2$ modes have to be kept to get a qualitatively correct picture. In order to keep the computing time at a reasonable level we use the $N = M = 2$ truncation in all following results.

The symmetric $M^{(n,m)}$ branch bifurcating at D2 and B2 is reproduced in figure 16(*b*). Figures 16(*a*) and 16(*c*) depict the variation of this branch with different streamwise wavenumbers α at the same Reynolds number $Re_p = 5000$. These results all have in common, that the fluctuation energy E as well as the corresponding friction factor c_f reach a maximum at the two-dimensional upper branch, i.e. at point D2 in figure 16(*b*). However, we hasten to add that we also computed antisymmetric $M^{(n,m)}$ branches which are not shown here. While these antisymmetric $M^{(n,m)}$

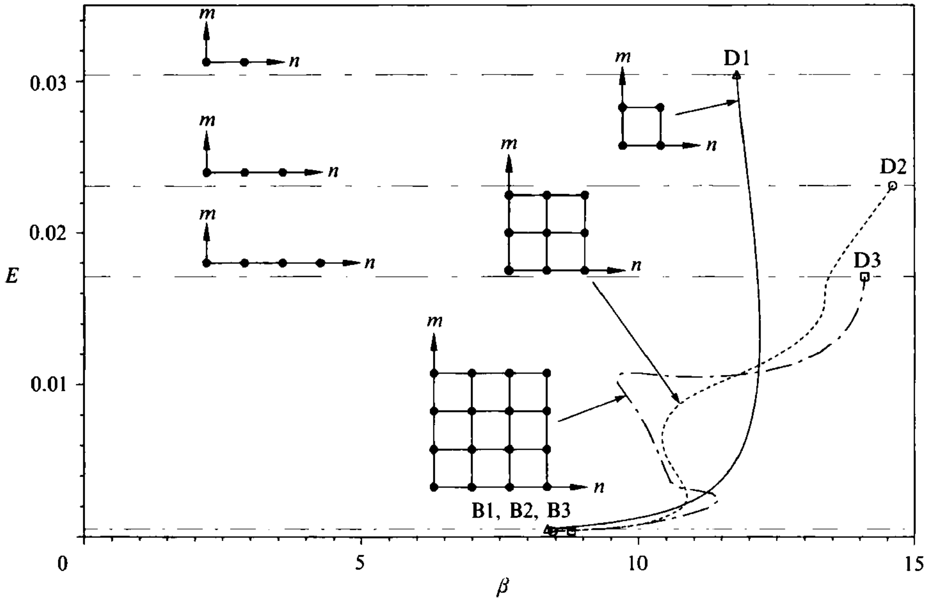

FIGURE 15. $Re_p = 5000$, $\alpha = 1.12$ cuts through symmetric secondary $M^{(n,m)}$ equilibrium surface of the most unstable mode σ_1 with $K = 15$ and various truncations $N = M$.

branches seem to follow the symmetric $M^{(n,m)}$ branches fairly closely over most of the parameter range, rather large deviations occur near the upper two-dimensional branch. These deviations are very similar to those observed for the $M^{(n,2m)}$ branches to be discussed in the following section. The fluctuation energy as well as the friction factor of the deviating parts of the antisymmetric solution, which can even form isolated branches, reaches values which are considerably above those of the nonlinear two-dimensional solution. Therefore we cannot exclude the existence of isolated symmetric $M^{(n,m)}$ branches with higher c_f values. If such isolated symmetric $M^{(n,m)}$ branches exist, they can only be reached via different parameter combinations. This matter is still to be investigated further. From the results obtained so far we conclude that the $M^{(n,2m)}$ solutions, to be discussed in the next section, are more important from a physical point of view.

4.2.2. *Secondary bifurcation solutions* $M^{(n,2m)}$ *containing only even spanwise Fourier modes*

In the search for solution branches with higher c_f values we investigated higher-order bifurcation points. Excluding the whole-channel problem, bicritical points, i.e. points where two neutral secondary instability modes coincide, turned out to exist also within the class of symmetric (and antisymmetric) solutions if one truncates at $N = M \geqslant 2$. The second unstable phase-locked mode σ_2 of figure 13(*b*) seemed to be an especially promising candidate for achieving such a coalescence. Therefore, truncating at $N = 2$ and keeping $Re_p = 5000$ fixed, we varied α and β but could not find any (α, β) combination for which the neutral points E2 and D2 of figure 13 coincided.

Another possibility for the creation of bicritical points are superharmonic bifurcation branches. Truncating at least at $N = M = 2$ the first spanwise harmonic (i.e. $m = 2$) phase-locked neutral mode of σ_1 bifurcates at point D2/2 in figure 16(*b*) with $\frac{1}{2}\beta_{\text{neut}}(\sigma_1)$ being half the β-value of point D2. Point D2/2 is fairly close to the neutral

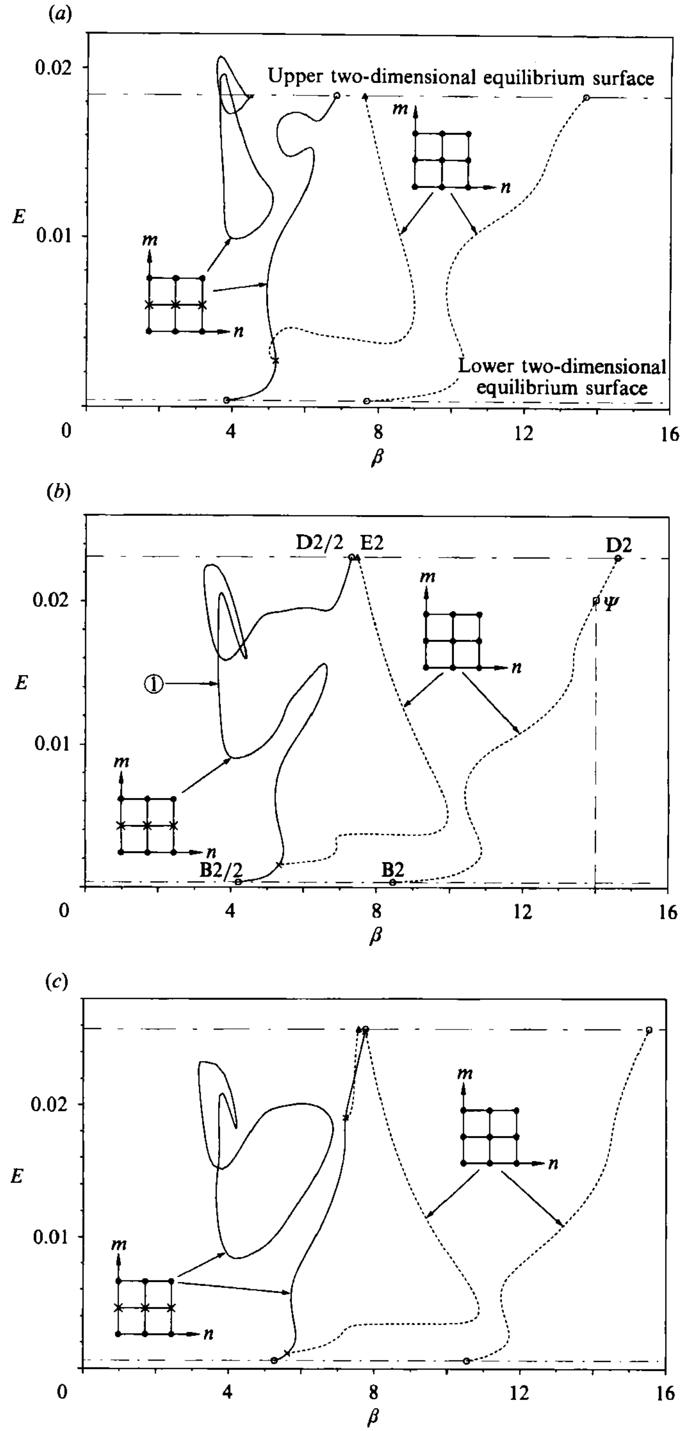

FIGURE 16. α = constant cuts through various secondary equilibrium surfaces with $Re_p = 5000$, $K = 15$ and $N = M = 2$: (*a*) $\alpha = 1.05$, (*b*) $\alpha = 1.12$ and (*c*) $\alpha = 1.2$. ——, $M^{(n,2m)}$ branch; ---, symmetric $M^{(n,m)}$ branch.

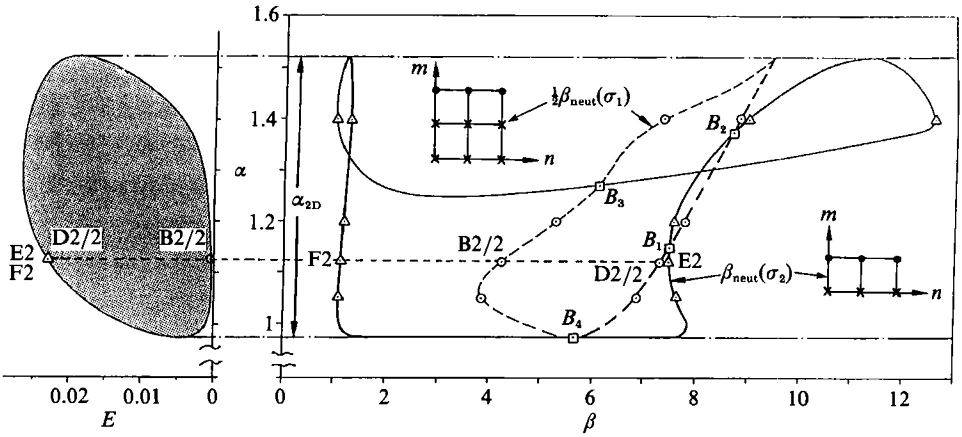

FIGURE 17. Curves of zero growth rate of the fundamental second unstable phase-locked mode $\beta_{neut}(\sigma_2)$ and the first spanwise harmonic of the first unstable phase-locked mode $\frac{1}{2}\beta_{neut}(\sigma_1)$ on the nonlinear two-dimensional equilibrium surface for $Re_p = 5000$, $K = 15$ and $N = 2$. The four bicritical points are marked $B_1, \ldots, B_4$.

point E2 of the second phase-locked mode σ_2. Therefore we tried next to vary the parameters Re_p and α such that these two neutral modes coincide.

We have done this in figure 17 by fixing $Re_p = 5000$ and varying only α as follows: the nonlinear two-dimensional equilibrium surface for $Re_p = 5000$ is a cylinder with its axis parallel to the β-axis and extending over the indicated α_{2D} range. The cross-section of the cylinder is shown on the left-hand side of figure 17. Fixing at first $\alpha = 1.12 =$ constant, the points where the second phase-locked mode σ_2 becomes neutral are F2 and E2 on the two-dimensional upper branch marked by triangles on the line $\alpha = 1.12 =$ constant. Halving the β values of D2 and B2, where the first phase-locked mode σ_1 has zero growth rate, we obtain the two points D2/2 on the two-dimensional upper branch and B2/2 on the two-dimensional lower branch indicated by circles. If we perform the same procedure for different α-values and connect the corresponding points in the (α, β)-plane of figure 17 we find two curves on the two-dimensional equilibrium cylinder: the solid curve $\beta_{neut}(\sigma_2)$ is the projection of the bifurcation points of the $M^{(n,m)}$ branch corresponding to the σ_2 mode. The dashed curve $\frac{1}{2}\beta_{neut}(\sigma_1)$ represents the projection of the $M^{(n,2m)}$ branch corresponding to the σ_1 mode. We observe that for these parameters there exist four intersection points B_1, B_2, B_3 and B_4 of the solid curve with the dashed curve on the two-dimensional equilibrium cylinder. These four points are marked by squares in figure 17 and constitute bicritical points. The two points B_1 and B_2 lie on the upper two-dimensional branch, B_3 is on the lower two-dimensional branch and B_4 is more or less at the connection of these two branches.

A local bifurcation analysis for point B_1 ($\alpha \approx 1.1485$, $\beta \approx 7.47$) via Lyapunov–Schmidt reduction showed interesting results (cf. Ehrenstein & Koch 1989, 1991) with possible mode interactions between the $M^{(n,m)}$ and $M^{(n,2m)}$ branches. The results of the global bifurcation analysis are shown in figure 16 for $Re_p = 5000$. Fixing at first $\alpha = 1.12$ (cf. figure 16*b*), we see that the spanwise superharmonic $M^{(n,2m)}$ branch of σ_1, bifurcating at D2/2 and depicted as solid curve, looks similar to the $M^{(n,m)}$ branch of σ_1, bifurcating at D2 and treated in the previous section, with the exception of a large 'bulge' near point D2/2. This 'bulge' drew our particular attention because the friction factor c_f of this part of the $M^{(2,2m)}$ branch surpasses by far the nonlinear two-dimensional values even though the fluctuation energy E in figure 16(*b*) remains

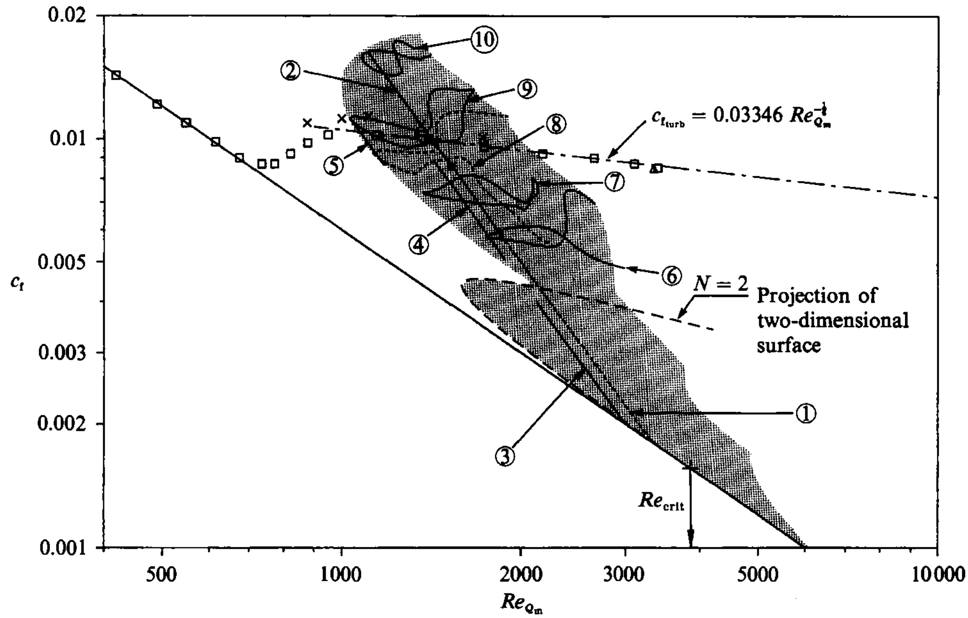

FIGURE 18. Friction factor c_f as function of Re_{Q_m} for various cuts through the secondary equilibrium surface $M^{(n,2m)}$ of σ_1 with $K = 15$ and $N = M = 2$. The approximate extent of the projection of the four-dimensional $M^{(n,2m)}$ surface is indicated by the shaded area. ---, projection of two-dimensional equilibrium surface for $N = 2$, $M = 0$, $\times$, three-dimensional low resolution simulation of Rozhdestvensky & Simakin (1984) with $N = M = 4$, $\triangle$, high resolution simulation of Gilbert (1988) with $N = M = 128$, $\square$, Patel & Head's (1969) experiment. The various cuts are: (1) $Re_p = 5000$, $\alpha = 1.12$; (2) $Re_p = 5000$, $\beta = 4$; (3) and (4) $Re_p = 4500$, $\alpha = 1.12$; (5) $Re_p = 3000$, $\beta = 4$; (6) $\alpha = 1.25$, $\beta = 6.25$; (7) $\alpha = 1.3$, $\beta = 5.5$; (8) $\alpha = 1.25$, $\beta = 4$; (9) $\alpha = 1.4$, $\beta = 4$; (10) $\alpha = 1.85$, $\beta = 4$.

below the two-dimensional value. This is demonstrated in figure 18, where the $M^{(n,2m)}$ branch (1) of figure 16(*b*) extends from the lower two-dimensional branch all the way up to the point near the turbulent value marked by a star, before ending on the upper two-dimensional branch. On the other hand the $M^{(n,m)}$ mode of σ_2, bifurcating at point $E2$ on the upper two-dimensional branch, see figure 16(*b*), ends on the $M^{(n,2m)}$ branch (1) near the lower two-dimensional branch. However, the corresponding c_f values remain below those of the two-dimensional equilibrium solution.

If we now vary α, say $\alpha = 1.05$ in figure 16(*a*) or $\alpha = 1.2$ in figure 16(*c*), we see that the $M^{(n,2m)}$ branch (1) of figure 16(*b*) can be continued to isolated branches which all have the remarkable property that the friction factor c_f of this isolated section can reach values far above those of the two-dimensional solution. We therefore believe that the $M^{(n,2m)}$ branches might be of importance in the transition process and could lead to a better transition criterium.

In addition to the $Re_p = 5000$ and $\alpha = 1.05$, 1.12, 1.2 cuts we computed various other cuts through the four-dimensional equilibrium surface. These various cuts are marked by encircled numbers in the c_f, Re_{Q_m} plot of figure 18. The corresponding curves are also shown in figure 19 where Re_p is plotted as a function of Re_{Q_m}. The approximate extent of the projection of the four-dimensional $M^{(n,2m)}$ surface of the σ_1 mode is outlined by the shaded area in both figures and allows a comparison with experimental and time-dependent simulation results. For completeness the projection of the two-dimensional equilibrium surface with $N = 2$ is also included as dashed curve.

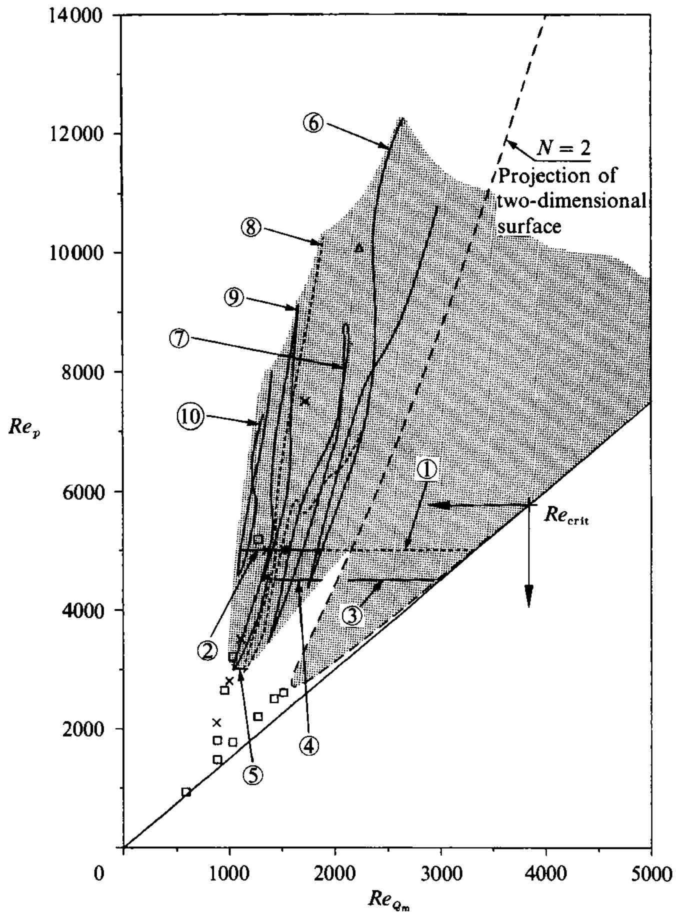

FIGURE 19. Re_p vs. Re_{Q_m} for various cuts through the secondary equilibrium surface $M^{(n,2m)}$ of σ_1 with $K = 15$ and $N = M = 2$. The approximate extent of the projection of the four-dimensional $M^{(n,2m)}$ surface is indicated by the shaded area. ---, projection of two-dimensional equilibrium surface for $N = 2$, $M = 0$. ×, three-dimensional low resolution simulation of Rozhdestvensky & Simakin (1984) with $N = M = 4$, □, Tillmann's experiment, see Herbert (1977), △, Eckelmann's (1970) experiment. Cuts as in figure 18.

The $M^{(n,2m)}$ solutions of the first unstable mode σ_1 apparently only exist for higher values of β and hence a direct comparison with a time-dependent simulation cited in the literature was possible only for Rozhdestvensky & Simakin's (1984) low resolution ($N = M = 4$) result for $Re_p = 5000$, $\alpha = 1.25$ and $\beta = 4$. Our corresponding result for c_f with $N = M = 2$ is the intersection of line ② with curve ⑧ in figure 18 which is fairly close to the cross marking Rozhdestvensky & Simakin's (1984) chaotic solution. In addition we note that in figure 18 some of our solutions like cut ② or cut ⑩ lead to c_f values which are considerably above the turbulent c_f values. One reason for this 'overshoot' could be the insufficient number of retained Fourier modes, i.e. $N = M = 2$. On the other hand this could be an actual property of this family of 'vortical' states. As will be documented later, the streamwise mean flow profiles of these $M^{(n,2m)}$ solutions show a certain similarity with the mean flow profiles of Gilbert's (1988) simulation results during the spike stage. In his time-dependent simulation Gilbert also observed an overshoot of c_f during the spike stage, see Gilbert's (1988) figure 7. In general we observe that the c_f values of the $M^{(n,2m)}$ branch

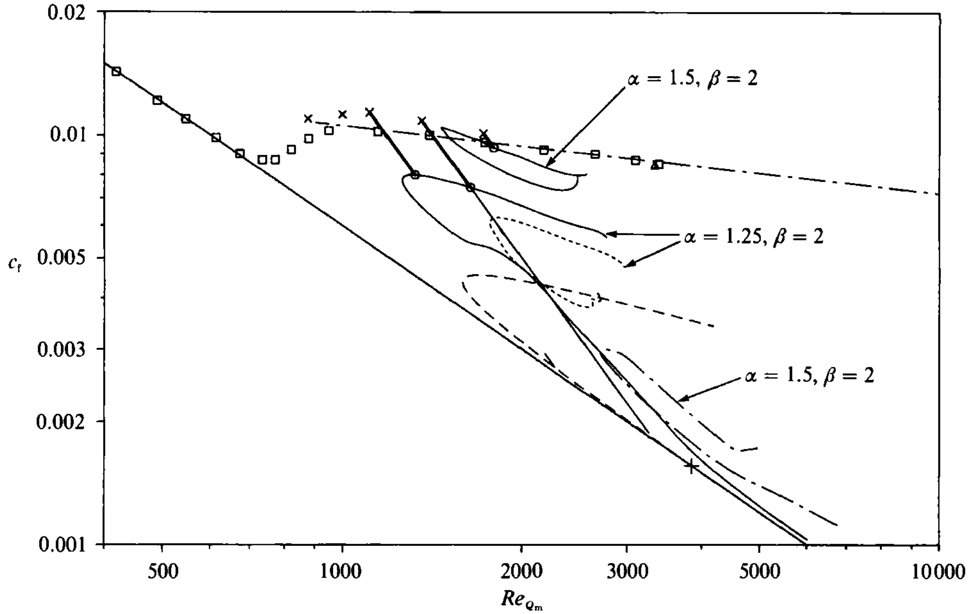

FIGURE 20. Friction factor c_f as function of Re_{Q_m} for various cuts through the secondary equilibrium surface $M^{(n,2m)}$ of σ_2 with $K = 15$ and $N = M = 2$. Comparison with $\times$, the low-resolution ($N = M = 4$) simulation of Rozhdestvensky & Simakin (1984) and $\square$, Patel & Head's (1969) experiment.

of σ_1 are surprisingly close to the turbulent mean values and that the critical Reynolds number of this solution class is reduced considerably, reaching $Re_{Q_m} \sim 1000$ which agrees with the experimentally observed values. Furthermore, all these three-dimensional equilibrium solutions show a strong subcritical character with rather high threshold amplitudes.

The restriction of $M^{(n,2m)}$ solutions to higher values of β in Ehrenstein & Koch (1989) can be eliminated by including the $M^{(n,2m)}$ branches of the second unstable phase-locked mode σ_2 bifurcating at $\frac{1}{2}\beta_{\text{neut}}(\sigma_2)$. Several such cuts through the four-dimensional $M^{(n,2m)}$ equilibrium surface of σ_2 have been computed and are shown in figure 20. With these results for lower values of β a comparison with the chaotic results of Rozhdestvensky & Simakin (1984) is possible. (We only note that contrary to our $N = M = 2$ truncation they truncated at $N = M = 4$.) This comparison is shown in figure 20 for three examples. Although such a comparison does not make sense in general because we are comparing a periodic solution with a chaotic solution, such a comparison is of considerable interest if one wants to find a better transition criterion which uses the simplest possible solution. In this sense we note that our periodic results, marked by circles in figure 20, are surprisingly close to the experimental results of Patel & Head (1969), marked by squares, as well as to the numerical simulation results of Rozhdestvensky & Simakin (1984), marked by crosses.

To gain additional insight we plotted the spanwise and streamwise averaged disturbance streamlines (in the moving frame of reference) together with the mean velocity profiles for various secondary equilibrium branches. The spanwise averaged (i.e. keeping only the $(n, 0)$ Fourier modes) disturbance streamlines closely resemble those of the two-dimensional solution, i.e. figure 7. The streamwise averaged (i.e. keeping only the $(0, m)$ Fourier modes) disturbance streamlines clearly demonstrate the essential difference between $M^{(n,m)}$ and $M^{(n,2m)}$ solution branches. A typical

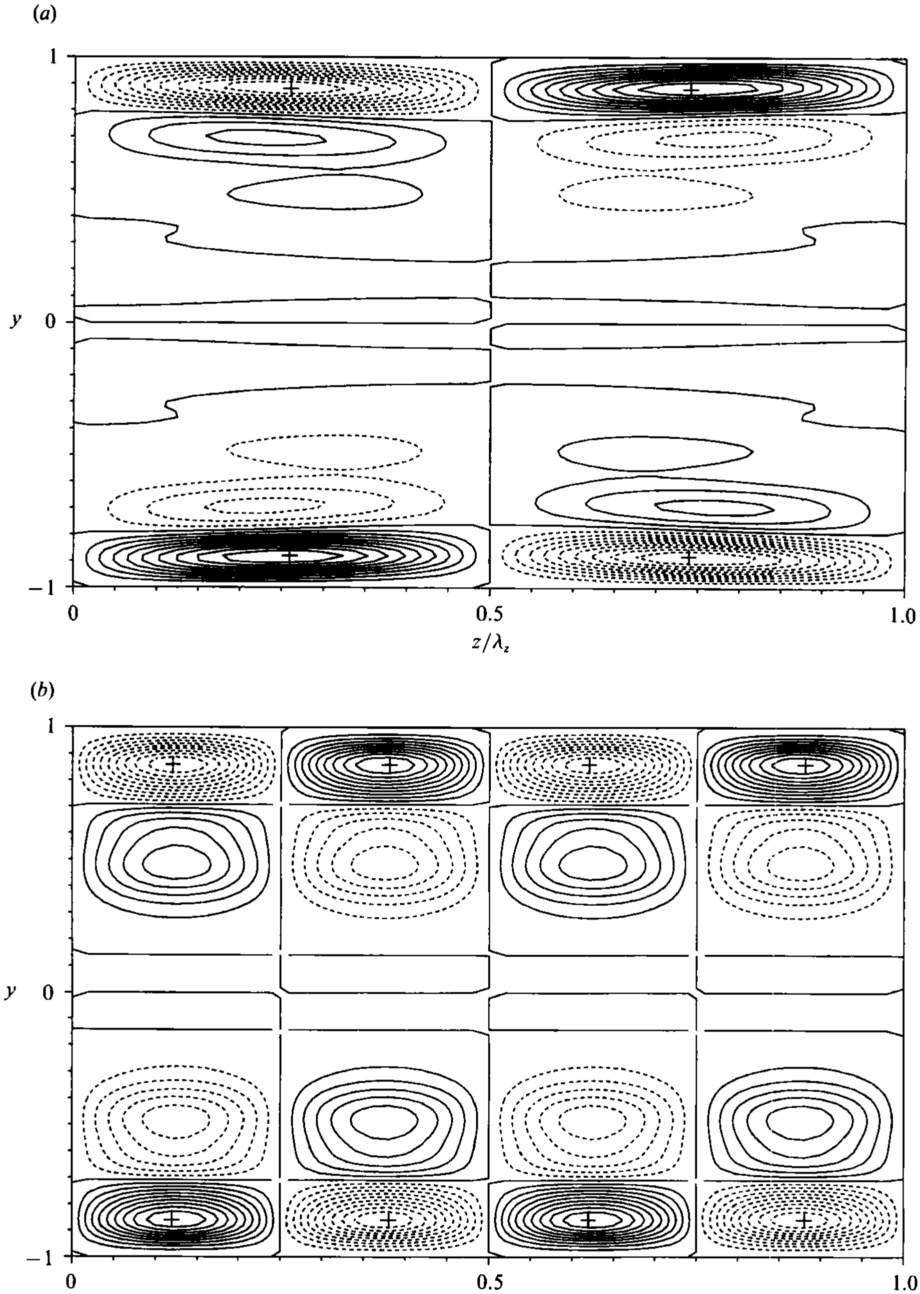

FIGURE 21. Streamwise averaged disturbance streamlines ($\Delta\psi = \frac{1}{20}[\psi_{max} - \psi_{min}]$) for $Re_p = 5000$, $K = 15$ and $N = M = 2$: (*a*) $M^{(n,m)}$ solution corresponding to conditions Ψ in figure 16(*b*) with $\alpha = 1.12$, $\beta = 14$, $E = 2.015 \times 10^{-2}$, $C = 0.2974$. (*b*) $M^{(n,2m)}$ solution corresponding to $\alpha = 1.8$, $\beta = 4$, $E = 9.303 \times 10^{-3}$, $C = 0.2195$.

$M^{(n,m)}$ solution, corresponding to the conditions denoted by Ψ in figure 16(*b*), is depicted in figure 21(*a*). Characteristic are the two streamwise vortices per spanwise wavelength. The corresponding mean velocity profile, depicted in figure 22(*a*), is still very similar to the one for the two-dimensional upper branch solution.

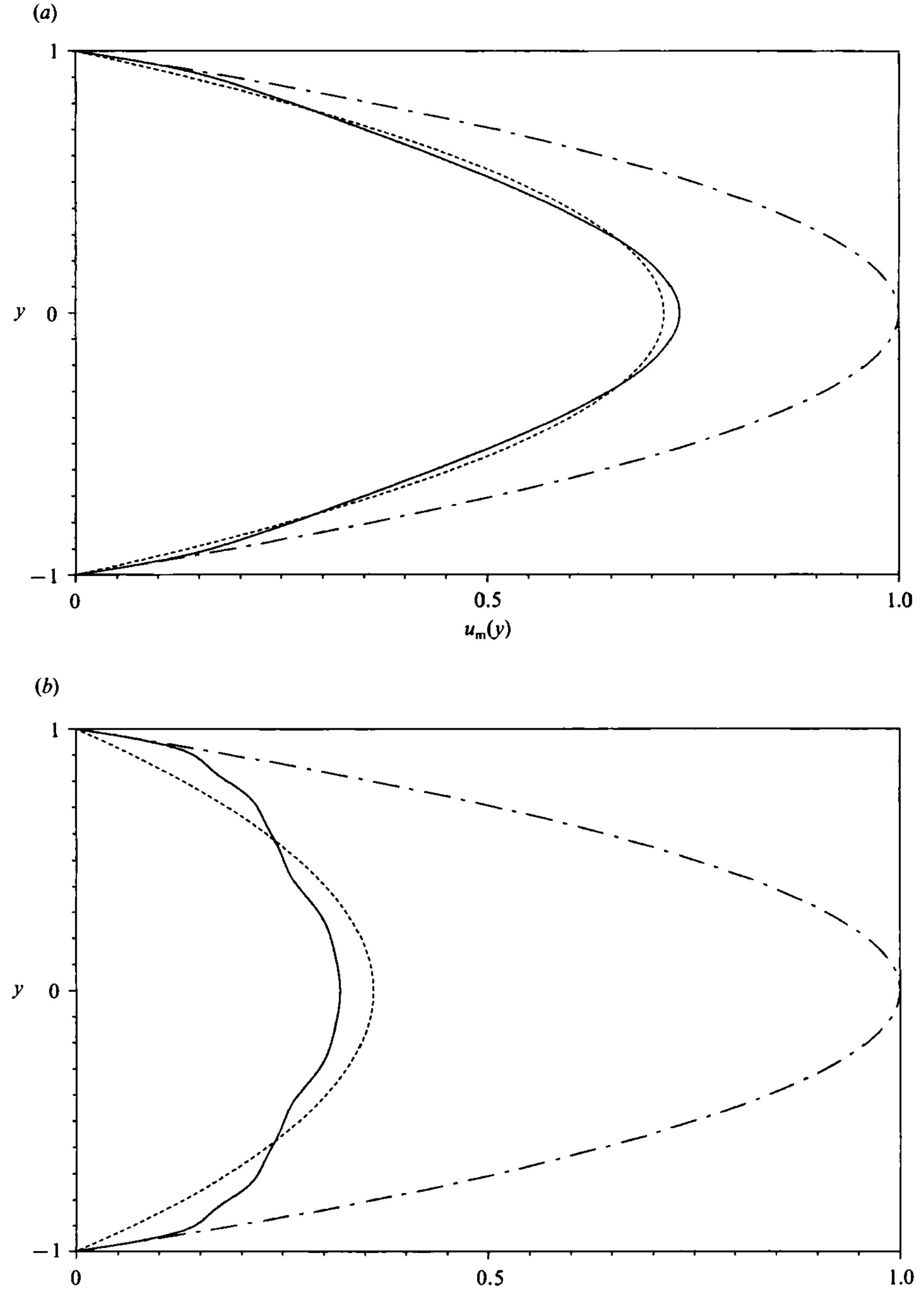

FIGURE 22. ——, mean velocity profiles $u_m(y)$ for $Re_p = 5000$: (*a*) $M^{(n,m)}$ solution corresponding to conditions Ψ in figure 16(*b*) with $\alpha = 1.12$, $\beta = 14$, $E = 2.015 \times 10^{-2}$, $C = 0.2974$. (*b*) $M^{(n,2m)}$ solution corresponding to $\alpha = 1.8$, $\beta = 4$, $E = 9.303 \times 10^{-3}$, $C = 0.2195$. Also included are the laminar flow parabolas for —·—, equal pressure gradient and ---, equal flux.

Contrary to this the $M^{(n,2m)}$ solutions, being spanwise harmonics, contain twice as many streamwise vortices per spanwise wavelength. This is demonstrated by the example of figure 21 (*b*). It is extremely interesting to note that the mean flow profile of this $M^{(n,2m)}$ solution, depicted in figure 22 (*b*), has a certain similarity with the profiles observed by Gilbert (1988) during the 'spike' stage in his time-dependent numerical simulation. This similarity is also apparent in the streamwise averaged streamline pictures of figure 21. The $M^{(n,m)}$ solution of figure 21 (*a*) is characteristic for the initial stage of transition, while the $M^{(n,2m)}$ solution of figure 21 (*b*) is similar to Gilbert's (1988) streamline plots (his figure 18) during the 'spike' stage. The number of streamwise vortices per channel cross-section varies for different branches, however no classification has been attempted here. A further characteristic of the 'spike' stage, namely the dominance of the (0, 2) mode (compare Gilbert's (1988) figure 11) is also found in $M^{(n,2m)}$ solutions. Therefore in our opinion the $M^{(n,2m)}$ solution branches are somehow related to the 'spike' stage of transition and might potentially be used for obtaining a more physically relevant transition criterion.

We conclude with a final remark, concerning the observation that the projections of the $M^{(n,2m)}$ solutions in figures 18 and 20 do not cover the transitional regime below $Re_{Q_m} \approx 1000$. As observed by Nishioka & Asai (1985) only intermittent flow has been found in this regime and perhaps no periodic equilibrium solutions are possible there. However quasi-periodic solutions might exist, requiring a solution for non-wavelike equilibrium branches as suggested by Pugh (1987). These solutions correspond to the non-phase-locked secondary instability modes shown in figure 13, but are much more difficult to compute.

5. Conclusions

Using Keller's (1977) pseudo-arclength continuation procedure, nonlinear three-dimensional travelling-wave type equilibrium solutions have been computed for plane Poiseuille flow. These travelling-wave type solutions originate at the neutral points of phase-locked secondary instability modes on the nonlinear primary bifurcation branch. Taking advantage of symmetries, only the solution branches corresponding to the symmetric and antisymmetric secondary instability modes have been considered. Of particular interest is the discovery of a new family of secondary bifurcation branches, termed $M^{(n,2m)}$, which contains only even spanwise Fourier modes. Largely dominated by the (0, 2) mode, these $M^{(n,2m)}$ solution branches raised the friction factor substantially to experimentally observed levels and at the same time reduced the critical Reynolds number to $Re_{Q_m} \approx 1000$. Furthermore, these new equilibrium solutions show characteristics usually observed during the 'spike' stage of transition and therefore are of potential use for improved transition prediction.

A distinctive feature of the new $M^{(n,2m)}$ equilibrium solutions is that they contain twice as many streamwise vortices per spanwise wavelength as the $M^{(n,m)}$ equilibrium solutions. The friction factor of the $M^{(n,2m)}$ branches is in general higher than that of the $M^{(n,m)}$ branches. Apparently the decreased vortex spacing is the reason for the higher friction factor of the $M^{(n,2m)}$ solutions. It is therefore plausible to assume that a reduction of the friction factor could be accomplished by suppressing the $M^{(n,2m)}$ solution and forcing the $M^{(n,m)}$ solution. Perhaps this could offer a possible explanation for the effect of drag-reducing riblets, which apparently also increase the spacing of low-speed streaks in the near-wall region, cf. Bacher & Smith (1986). At present this observation is rather speculative and not substantiated by any experimental results in plane Poiseuille flow. However the bifurcation analysis is presently being extended to two-dimensional boundary-layer flows where a comparison with experimental results might be possible.

The authors are indebted to Dr L. Kleiser and Dr T. Fischer for stimulating and helpful discussions, especially at the beginning of this study, and to Mr L. Leopold for producing the many computer plots. Also the constructive criticism of the referees is gratefully acknowledged.

REFERENCES

AGARD Conference Proceedings 1977 Laminar–turbulent transition. AGARD-CP-224.

BACHER, E. V. & SMITH, C. R. 1986 Turbulent boundary-layer modification by surface riblets. *AIAA J.* **24**, 1382–1385.

BAYLY, B. J., ORSZAG, S. A. & HERBERT, T. 1988 Instability mechanisms in shear-flow transition. *Ann. Rev. Fluid Mech.* **20**, 359–391.

BENNEY, D. J. 1964 Finite amplitude effects in an unstable laminar boundary layer. *Phys. Fluids* **7**, 319–326.

BENNEY, D. J. & LIN, C. C. 1960 On the secondary motion induced by oscillations in a shear flow. *Phys. Fluids* **3**, 656–657.

BUSHNELL, D. M., MALIK, M. R. & HARVEY, W. D. 1989 Transition prediction in external flows via linear stability theory. In *IUTAM Symposium Transsonicum III* (ed. J. Zierep & H. Oertel), pp. 225–242. Springer.

CANUTO, C., HUSSAINI, M. Y., QUARTERONI, A. & ZANG, T. A. 1988 *Spectral Methods in Fluid Dynamics*. Springer.

CHEN, T. S. & JOSEPH, D. D. 1973 Subcritical bifurcation of plane Poiseuille flow. *J. Fluid Mech.* **58**, 337–351.

CRAIK, A. D. D. 1971 Nonlinear resonant instability in boundary layers. *J. Fluid Mech.* **50**, 393–413.

CRAIK, A. D. D. 1985 *Wave Interactions and Fluid Flows*. Cambridge University Press.

CROUCH, J. D. & HERBERT, T. 1986 Perturbation analysis of nonlinear secondary instability in boundary layers. *Bull. Am. Phys. Soc.* **31**, 1718.

DEISSLER, R. J. 1987 The convective nature of instability in plane Poiseuille flow. *Phys. Fluids* **30**, 2303–2305.

DHANAK, M. R. 1983 On certain aspects of three-dimensional instability of parallel flows. *Proc. R. Soc. Lond.* A **385**, 53–84.

DOEDEL, E. 1981 Auto: a program for the automatic bifurcation analysis of autonomous systems. *Cong. Num.* **30**, 265–284.

DRAZIN, P. G. & REID, W. H. 1981 *Hydrodynamic Stability*. Cambridge University Press.

ECKELMANN, H. 1970 Experimentelle Untersuchungen in einer turbulenten Kanalströmung mit starken viskosen Wandschichten. *Mitt. MPI für Strömungsforschung und AVA Göttingen* no. 48.

EHRENSTEIN, U. 1988 Lösung der linearen, inkompressiblen Stördifferentialgleichungen mittels Chebyshev–Kollokation. *Internal DFVLR-Rep.* IB 221-88 A 09.

EHRENSTEIN, U. & KOCH, W. 1989 Nonlinear bifurcation study of plane Poiseuille flow. *DLR Res. Rep.* FB 89-42.

EHRENSTEIN, U. & KOCH, W. 1991 Local and global analysis of secondary bifurcations in plane Poiseuille flow. To appear in the special issue of *European J. Mech.* B *Fluids* containing the *Proc. IUTAM Symp. Nonlinear Hydrodynamic Stability and Transition, Sept. 3–7, 1990, Sophia-Antipolis, France.*

GILBERT, H. 1988 Numerische Simulation der Transition von der laminaren in die turbulente Kanalströmung. *DFVLR Res. Rep.* FB 88-55.

GOLDSHTIK, M. A., LIFSHITS, A. M. & SHTERN, V. N. 1983 The Reynolds number in a transition in a plane channel. *Sov. Phys. Dokl.* **28**, 923–925.

GOLUBITZKY, M., STEWART, I. & SCHAEFFER, D. G. 1988 *Singularities and Groups in Bifurcation Theory*, vol. 2. Springer.

GOTTLIEB, D., HUSSAINI, M. Y. & ORSZAG, S. A. 1984 Theory and applications of spectral methods. In *Spectral Methods for Partial Differential Equations* (ed. R. G. Voigt, D. Gottlieb & M. Y. Hussaini), pp. 1–54. SIAM Philadelphia.

GROHNE, D. 1969 Die Stabilität der ebenen Kanalströmung gegenüber dreidimensionalen Störungen von endlicher Amplitude. *AVA Göttingen, Rep.* 69 A 30.

HERBERT, T. 1977 Die Neutralfläche der ebenen Poiseuilleströmung. Habilitationsschrift, Universität Stuttgart.

HERBERT, T. 1980 Nonlinear stability of parallel flows by high-order amplitude expansions. *AIAA J.* **18**, 243–248.

HERBERT, T. 1981 A secondary instability mechanism in plane Poiseuille flow. *Bull. Am. Phys. Soc.* **26**, 1257.

HERBERT, T. 1983 On perturbation methods in nonlinear stability theory. *J. Fluid Mech.* **126**, 167–186.

HERBERT, T. 1984 Modes of secondary instability in plane Poiseuille flow. In *Turbulence and Chaotic Phenomena in Fluids* (ed. T. Tatsumi), pp. 53–58. North-Holland.

HERBERT, T. 1988 Secondary instability of boundary layers. *Ann. Rev. Fluid Mech.* **20**, 487–526.

HERBERT, T. 1991 Exploring transition by computer. *Appl. Num. Maths.* **7**, 3–25.

JEPSON, A. D. & KELLER, H. B. 1984 Steady state and periodic solution paths: their bifurcations and computations. In *Numerical Methods for Bifurcation Problems* (ed. T. Küpper, H. D. Mittelmann & H. Weber), pp. 219–246. Birkhäuser.

JIMÉNEZ, J. 1987*a* Coherent structures and dynamical systems. In *Proc. 1987 Summer Program of the NASA Stanford Center for Turbulence Res. Rep.* CTR-S87, pp. 323–324.

JIMÉNEZ, J. 1987*b* Bifurcations and bursting in two-dimensional Poiseuille flow. *Phys. Fluids* **30**, 3644–3646.

JIMÉNEZ, J. 1990 Bifurcations and turbulence in plane Poiseuille flow. In *Near-Wall Turbulence. 1988 Zoran Zaric Memorial Conference* (ed. S. J. Kline & N. H. Afgan), pp. 28–44. Hemisphere.

KACHANOV, YU. S. & LEVCHENKO, V. YA. 1984 The resonant interaction of disturbances at laminar–turbulent transition in a boundary layer. *J. Fluid Mech.* **138**, 209–247.

KELLER, H. B. 1977 Numerical solution of bifurcation and nonlinear eigenvalue problems. In *Applications of Bifurcation Theory* (ed. P. H. Rabinowitz), pp. 359–384. Academic Press.

KIM, J., MOIN, P. & MOSER, R. 1987 Turbulence statistics in fully developed channel flow at low Reynolds number. *J. Fluid Mech.* **177**, 133–166.

KLEBANOFF, P. S., TIDSTROM, K. D. & SARGENT, L. M. 1962 The three-dimensional nature of boundary-layer instability. *J. Fluid Mech.* **12**, 1–34.

KLEISER, L. & ZANG, T. A. 1991 Numerical simulation of transition in wall-bounded shear flows. *Ann. Rev. Fluid Mech.* **23**, 495–537.

KOCH, W. 1988 Nonlinear limit-cycle solutions – a rational method for transition prediction in shear flows? In *Propagation in Systems far from Equilibrium* (ed. J. E. Wesfreid, H. R. Brand, P. Manneville, G. Albinet & N. Boccara), pp. 360–368. Springer.

KUBIČEK, M. & MAREK, M. 1983 *Computational Methods in Bifurcation Theory and Dissipative Structures*. Springer.

LIU, J. T. C. 1989 Coherent structures in transitional and turbulent free shear flows. *Ann. Rev. Fluid Mech.* **21**, 285–315.

MAY, C. L. & KLEISER, L. 1985 Numerical simulation of subharmonic transition in plane Poiseuille flow. *Bull. Am. Phys. Soc.* **30**, 1748.

MEKSYN, D. 1964 Stability of laminar flow between parallel planes for two- and three-dimensional finite disturbances. *Z. Phys.* **178**, 159–172.

MEKSYN, D. & STUART, J. T. 1951 Stability of viscous motion between parallel planes for finite disturbances. *Proc. R. Soc. Lond.* A **208**, 517–526.

MEYER-SPASCHE, R. & KELLER, H. B. 1980 Computations of the axisymmetric flow between rotating cylinders. *J. Comp. Phys.* **35**, 100–109.

MILINAZZO, F. A. & SAFFMAN, P. G. 1985 Finite-amplitude waves in plane viscous shear flows. *J. Fluid Mech.* **160**, 281–295.

MORKOVIN, M. V. 1988 Recent insights into instability and transition to turbulence in open-flow systems. *AIAA paper* 88-3675 (also *ICASE Rep.* 88-44).

NISHIOKA, M. & ASAI, M. 1985 Some observations of the subcritical transition in plane Poiseuille flow. *J. Fluid Mech.* **150**, 441–450.

NISHIOKA, M., IIDA, S. & ICHIKAWA, Y. 1975 An experimental investigation of the stability of plane Poiseuille flow. *J. Fluid Mech.* **72**, 731–751.

ORSZAG, S. A. 1971 Accurate solution of the Orr–Sommerfeld stability equation. *J. Fluid Mech.* **50**, 689–703.

ORSZAG, S. A. & KELLS, L. C. 1980 Transition to turbulence in plane Poiseuille and plane Couette flow. *J. Fluid Mech.* **96**, 159–206.

ORSZAG, S. A. & PATERA, A. T. 1980 Subcritical transition to turbulence in plane channel flows. *Phys. Rev. Lett.* **45**, 989–993.

ORSZAG, S. A. & PATERA, A. T. 1983 Secondary instability of wall-bounded shear flows. *J. Fluid Mech.* **128**, 347–385.

PATEL, V. C. & HEAD, M. R. 1969 Some observations on skin friction and velocity profiles in fully developed pipe and channel flows. *J. Fluid Mech.* **38**, 181–201.

PEKERIS, C. L. & SHKOLLER, B. 1969 The neutral curves for periodic perturbations of finite amplitude of plane Poiseuille flow. *J. Fluid Mech.* **39**, 629–639.

PUGH, J. D. 1987 Finite amplitude waves in plane Poiseuille flow. Ph.D. thesis, California Institute of Technology.

PUGH, J. D. & SAFFMAN, P. G. 1988 Two-dimensional superharmonic stability of finite amplitude waves in plane Poiseuille flow. *J. Fluid Mech.* **194**, 295–307.

REED, H. L. & SARIC, W. S. 1989 Stability of three-dimensional boundary layers. *Ann. Rev. Fluid Mech.* **21**, 235–284.

RESHOTKO, E. 1976 Boundary-layer stability and transition. *Ann. Rev. Fluid Mech.* **8**, 311–349.

ROZHDESTVENSKY, B. L. & SIMAKIN, I. N. 1984 Secondary flows in a plane channel: their relationship and comparison with turbulent flows. *J. Fluid Mech.* **147**, 261–289.

SAFFMAN, P. G. 1983 Vortices, stability and turbulence. *Ann. N.Y. Acad. Sci.* **404**, 12–24.

SARIC, W. S. & THOMAS, A. S. W. 1984 Experiments on the subharmonic route to turbulence in boundary layers. In *Turbulence and Chaotic Phenomena in Fluids* (ed. T. Tatsumi), pp. 117–122. North-Holland.

SCHLICHTING, H. 1933 Zur Entstehung der Turbulenz bei der Plattenströmung. *Nachr. Ges. Wiss. Göttingen, Math. Phys. Kl.* 182–208.

SCHLICHTING, H. 1958 *Grenzschicht-Theorie* (3rd edn). Braun.

SCHRAUF, G. 1986 The first instability in spherical Taylor–Couette flow. *J. Fluid Mech.* **166**, 287–303.

SCHUBAUER, G. B. & SKRAMSTAD, H. K. 1947 Laminar boundary-layer oscillations and transition on a flat plate. *J. Res. Natl Bur. Stand.* **38**, 251–292 (reprint of *NACA Adv. Conf. Rep.* 1943).

SEN, P. K. & VENKATESWARLU, D. 1983 On the stability of plane Poiseuille flow to finite-amplitude disturbances, considering the higher-order Landau constants. *J. Fluid Mech.* **133**, 179–206.

SHTERN, V. N. 1976 Instability due to three-dimensional disturbances. *Izv. Akad. Nauk SSSR Mekh. Zhid. i Gaza*, **5**, 29–34.

SQUIRE, H. B. 1933 On the stability of three-dimensional disturbances of viscous flow between parallel walls. *Proc. R. Soc. Lond.* A **142**, 621–628.

STUART, J. T. 1960 On the nonlinear mechanics of wave disturbances in stable and unstable parallel flows. Part 1. The basic behaviour in plane Poiseuille flow. *J. Fluid Mech.* **9**, 353–370.

STUART, J. T. 1971 Nonlinear stability theory. *Ann. Rev. Fluid Mech.* **3**, 347–370.

TANI, I. 1969 Boundary-layer transition. *Ann. Rev. Fluid Mech.* **1**, 169–196.

TOLLMIEN, W. 1929 Über die Entstehung der Turbulenz. *Nachr. Ges. Wiss. Göttingen, Math. Phys. Kl.* 21–44.

Watson, J. 1960 On the nonlinear mechanics of wave disturbances in stable and unstable parallel flows. Part 2. The development of a solution for plane Poiseuille flow and for plane Couette flow. *J. Fluid Mech.* **9**, 371–389.

Zahn, J.-P., Toomre, J., Spiegel, E. A. & Gough, D. O. 1974 Nonlinear cellular motions in Poiseuille channel flow. *J. Fluid Mech.* **64**, 319–345.